4.1. Introduction

The 7075 Al-alloys have been widely used in the aerospace, aviation, armor, and automobile industries owing to a high specific strength, and work hardening exponent [11,90,202,211], which arises due to precipitation. There is an inseparable relationship between the precipitation and the strengthening mechanisms [212]. The precipitation sequence of 7xxx series Al-alloys with a higher Zn/Mg ratio (≥2) is given as supersaturated solid solution(α)-GP zone (coherent)-η'(semi-coherent)- η (incoherent, $MgZn_2$) [6–8]. The *GP zone*, and *η'* are major strengthening factors in the T6 temper [85]. Moreover, η causes high hardening in T73 [213]. Further, the inverse relationship between the strength-ductility trade-off between the T6, and T73 tempers are widely reported [85,214]. For instance, Rout et al. [88], reported high strength (YS ~400±5 MPa) but less ductility (*%EL~10*) in T6 tempered 7017 Al alloy. The T73 portrays enhanced ductility (*%EL~13*) than T6, but their YS decreases up to 313±2 MPa [88]. Cina et al. [215] developed the retrogression and re-aging (RRA) treatment to maintain the strength-ductility trade-off. However, this is unsuitable for materials with large profiles due to the short retrogression time embedded in the process. The matrix grain refinement techniques, following the SPD methods, for instance, accumulative roll bonding (ARB)[216], equal channel angular pressing (ECAP), and high-pressure torsion (HPT) [18,122,217,218], are given to improve the performances of the 7xxx series of Al-alloy. However, the challenges associated with producing large-scale parts provided practical limitations. Sufficient scientific investigation depicts that the cold rolling followed by ageing, just after solution quenching (solution quenching + cold rolling + peak-aging) has been proven the industrially feasible processing technique to improve the strength-ductility trade-off by refining the α-Al grains and increasing the dislocation density [212,219,220]. Such processing techniques also change the texture by activating the non-basal slip system.

For instance, the evolution of the Bs texture with increased intensity is observed by Zhao et al. [220 A] in the Al-Cu-Mg-based alloy. The Lin et al. [221], obtained an enhanced yield strength of 301 MPa, following the "pre-aging+ cold rolling+ peak-aging" process in an Al-Cu-Mg alloy system as compared to the conventional peak-aged alloy (*YS~248MPa*). Huo et al. [222], employed warm rolling and continuous rolling treatment in 7075 Al alloy to refine the grain size up to 10μm, thereby improving the mechanical properties. Zuo et al. [223], applied thermo-mechanical treatment in 7055 Al alloy, applying the pre-deformation, and short-time annealing just after subjecting the alloy to hot rolling for obtaining the ultra-fine-grain micro-structures, thereby improving mechanical properties. Ren et al. [13], invented another thermo-mechanical treatment, solution quenching (SQ)+room temperature asymmetric rolling (5%, and 10%) followed by the natural-aging treatment of 15 days, in 6xxx series of Al-alloys, thereby attaining the increased YS of 289 ±5 MPa, in comparison to YS of 206 ±3 MPa in the conventional form, while maintaining the ductility of 20%. Such strengthening arises due to the combined effect of solute clustering, dislocation, and textures. Chen et al. [31] applied another thermo-mechanical treatment in the Al-Zn-Mg-Cu alloy, following the hot rolling and the asymmetric rolling for obtaining the enhanced strength-ductility trade-off. The enhanced strength arises due to the combined effects of the dislocation, co-cluster formation, textures, and fine precipitates [30]. Whereas, the dislocation recovery is a major responsible factor for attaining the increased ductility [31]. The above-mentioned literature reviews and significant facts reported in a few pieces of the work depict enough scientific information of the thermo-mechanically processed 7xxx, 6xxx, and 2xxx-series of Al-alloys, as well as the Al-Zn-Mg-Cu based alloy systems. However, the thermo-mechanical treatment following the simplest and industrially feasible route e.g., solution quenching (SQ) + cold rolling (CR) + peak-aging (PA) of the 7075 Al-

alloys is lacking for the structure-property correlations. Current work, therefore, illustrates the complex interplay of the precipitation behavior, dislocation structures, texture, and mechanical properties of the cold rolled 7075 Al alloy to three different amounts of deformation, e.g., 15%, 30%, and 45% just after the solution quenching, which was followed by the peak ageing (24hrs, 120ºC).

4.2 Results

4.2.1 XRD analysis

Fig. 4.1a shows a combined XRD plot of the SQ and the peak-aged (T6) alloy. The top portion depicts the XRD pattern of SQ alloy, whereas the bottom portion depicts the T6 alloy. Analyzes of the XRD pattern only display sharp crystalline peaks (111, 200, 220, and 311) of the α-Al (a=4.04Å, cF4 structures) in the SQ state, and weak crystalline peaks of precipitates *(GP zone, η' and η)* are absent. On the other hand, weak crystalline peaks (002, 201, and 211) of precipitates *(η' and η)* are observed in the T6 condition, in addition to the sharp crystalline peaks of α-Al. Another minor crystalline peak (004) of Al_2CuMg, and (200) of Al_2Cu are also observed. Fig. 4.1a_1 portrays the magnified view in 2θ range of 39° to 43°section. The presence of *η' and η* phases are observed in T6 temper. On the other hand, no precipitates are seen in the SQ condition. Fig. 4.1a_2 illustrates the magnified view in 2θ range of 46.5° to 49.5°section. The presence of the η' and η phases are also found in the T6 condition but no significant peaks of η' and η are seen in the SQ state, keeping the intensity range constant. Shifting of the 200 peaks of α-Al also supports the precipitation after peak-ageing.

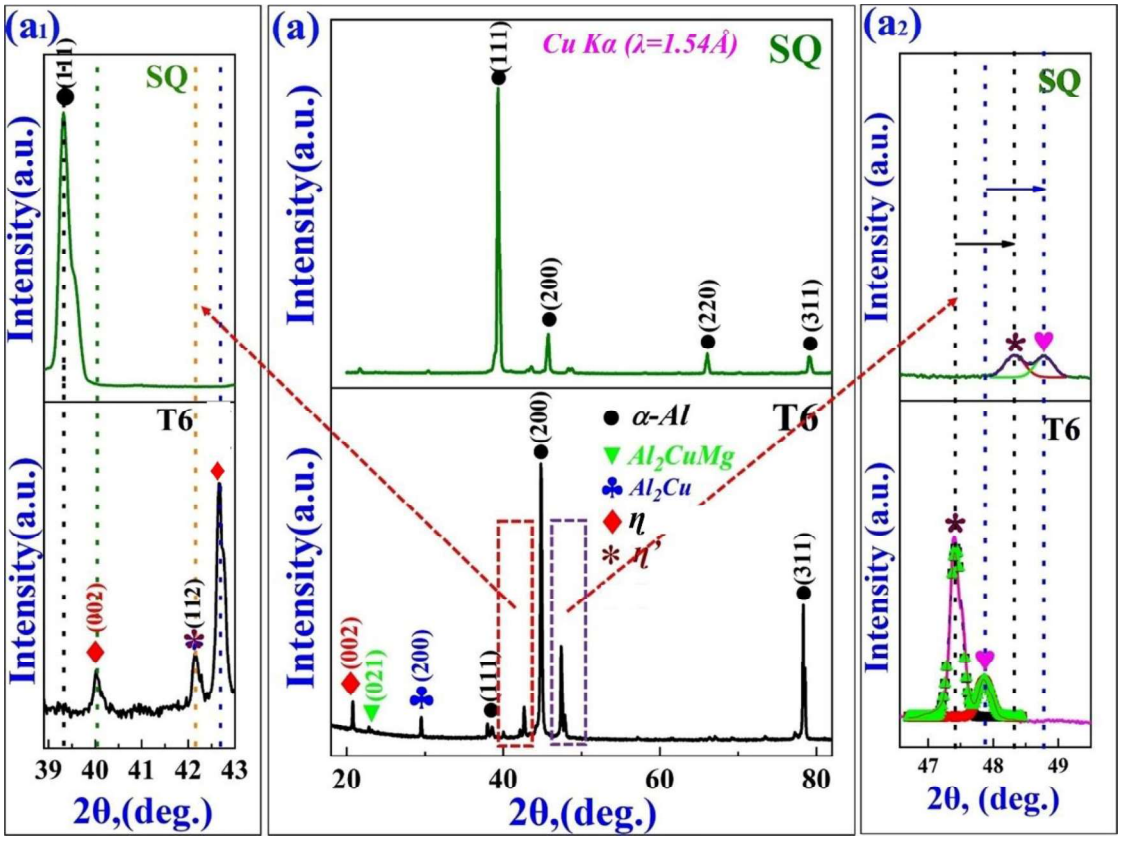

Figs. 4.1a XRD Peaks of heat treated (SQ, and T6) alloy: (a) 2θ range of 15° to 85°, (a_1) 2θ range of 39° to 43°, and (a_2) 2θ range of 46.5° to 49.5°.

Fig. 4.1b shows the XRD pattern of thermo-mechanically processed alloy, in TMP-1, TMP-2, and TMP-3 conditions. The top portion depicts the XRD patterns of TMP-1. Analyzes of the peaks show the presence of weak crystalline peaks of metastable *(η')*, and equilibrium *(η)* precipitates, in addition to sharp crystalline peaks of the α-Al. Volume fractions/ intensity of the GP zone is more in TMP-1, as compared to the T6 state, showing enhanced formation of the η precipitates. The middle portion shows the XRD pattern of TMP-2. The presence of the weak crystalline phases of η' and η are observed in addition to the sharp crystalline peaks of α-Al. The volume fraction of the η' is higher than the *η* in this state. The bottom portion displays the XRD pattern of TMP-3. Investigation of the peaks also shows sharp crystalline peaks of the α-Al, and the weak crystalline peaks of the, *η' and η*. The Intensity/ volume

fraction of the η is higher than the η'. Fig. 4.1b$_1$ shows an enlarged view of the XRD peak of 111 of the α-Al. This shows the shifting of the 111 peaks towards the left while increasing deformation on account of the thermo-mechanical processing. This also depicts changes in the lattice parameter of α-Al, on account of the deformation. Fig. 4.1b$_2$ depicts enlarge view of XRD peaks in 2θ range of 41.2° to 43.1°, and

Fig. 4.1b$_3$ shows an enlarged view of XRD peaks in 2θ range of 46.3° to 48.6°. Analysis of peaks shows the presence of weak crystalline phases of η' and η in both angular ranges for all the conditions but their volume fraction changes depending on the peak intensity or area under the peak. The volume fraction of η' is more for the TMP-1 and TMP-2. On the other hand, the volume fraction of the η phase is more for on TMP-3. The 111 peak of α-Al, is an intense peak, for the AR alloy and TMP-1. On the other hand, 200 is the preferred orientation for the TMP-2, and TMP-3 but the intensity of 200 reflections is higher for TMP-3, in comparison to TMP-2.

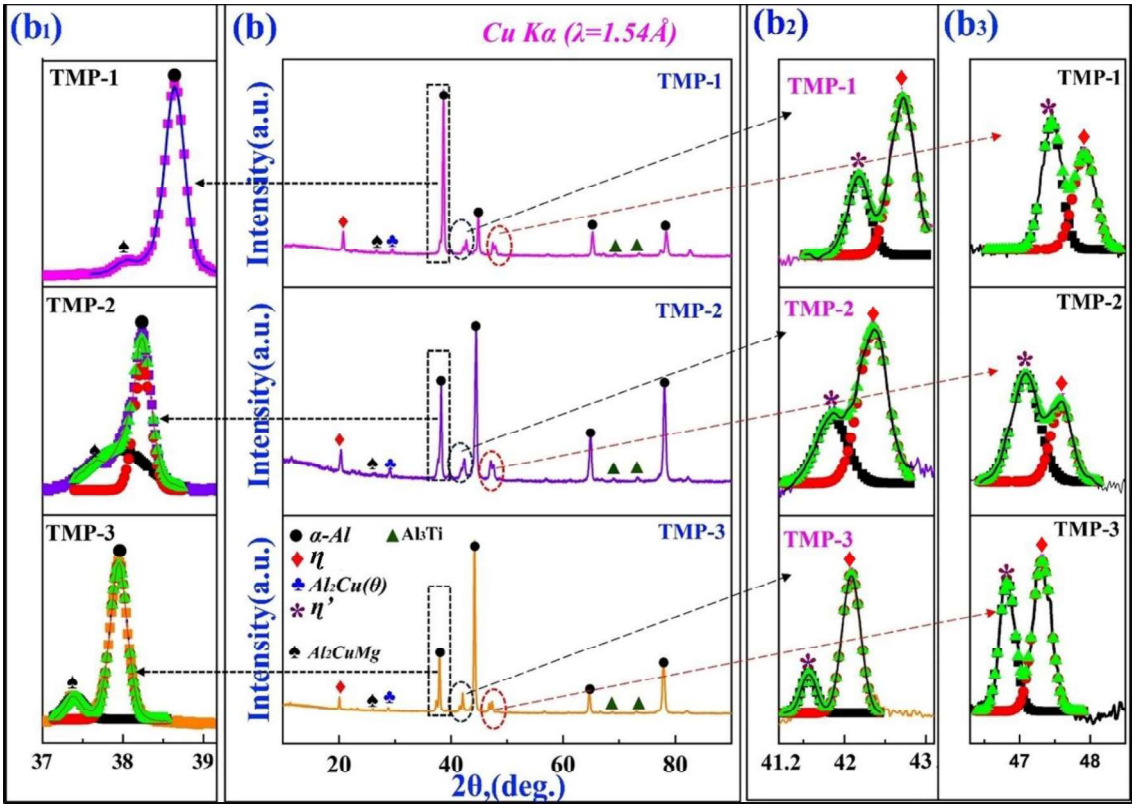

Fig. 4.1b XRD peaks after thermo-mechanical processing: (b) XRD peaks in 2θrange of 15° to 85°(full range), (b_1) magnified view of 111 reflection showing left shift from TMP-1 to TMP-3, (b_2) magnified view in 2θ range of 41.2° to 43°, (b_3) magnified view in 2θ range of 46.3° to 48.2°. The top shows TMP-1, the middle TMP-2, and the bottom depicts TMP-3.

Fig. 4.1c shows the magnified XRD peaks in the *2θ* range of 19.7° to 21.3° in the fixed intensity range. This clearly shows ηformation is more for the TMP-1, followed by the TMP-2 and TMP-3. Peak shifting towards the left also indicates the changes in the chemistry/ formation or dissolution of phases. The magnified XRD peaks in *2θ* range of 39.4° to 43.2° is shown in Fig. 4.1d. This clearly shows that the volume fraction of *η* is more in TMP-3. The presence of the *η* peak is also observed in TMP-1 as marked by the black arrow.

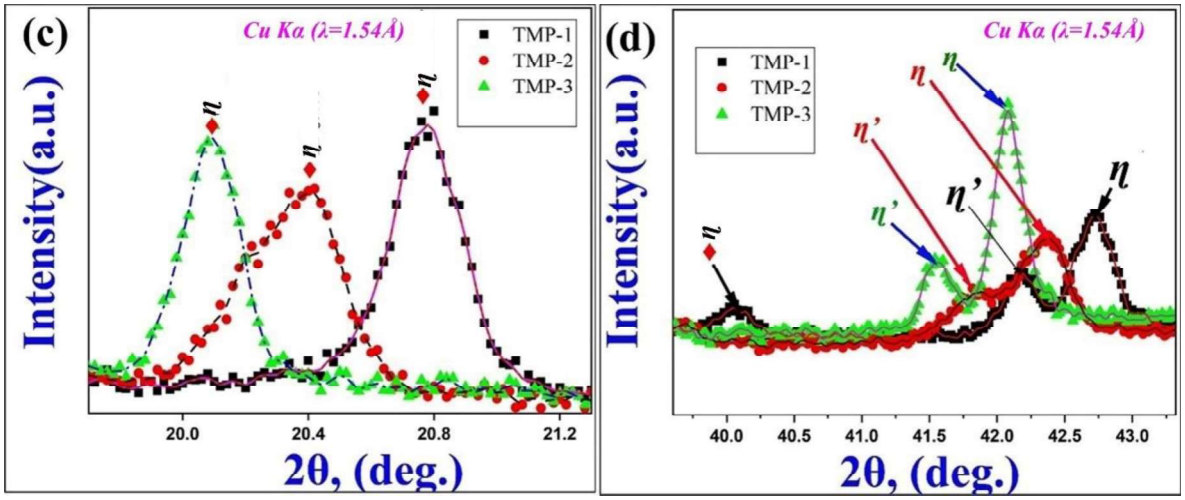

Fig. 4.1c-d XRD peaks of TMP-1, TMP-2 and TMP-3 in the angular range 2θ of 19.7° to 21.3°(c), and 2θ angular range of 39.5° to 43.5°(d).

The lattice microstrain (ε), crystallite size (D in Å), and dislocation density for all conditions are calculated using the major XRD reflection of α-Al, which is given in Table 4.1.

Table 4.1 Calculated lattice micro-strain, crystallite size, and dislocation density

Processing State	Lattice microstrain(ε)	Crystallite Size(D, *in Å*)	Dislocation density ($x10^{15}/m^2$)
Solution quenching (S.Q.)	.0850	20.5	6.8
Peak-aged (T6)	0.0704	20.18	1.6
TMP-1	0.2400	65.00	2.1
TMP-2	0.1000	13.50	3.0
TMP-3	0.1200	11.50	3.6

Among all the processed alloys, the high dislocation density ($68x10^{17}/m^2$), and crystallite size (d~70Å) were measured in the SQ state (Table 4.1). At the same time, the least crystallite size (*D, in Å*) and dislocation density are measured for the TMP-3. The volume fraction of precipitates is calculated following the standard procedures reported in the literature [224], and their values are given in Table 4.2.

Table 4.2 Volume fraction of precipitates after heat treatments and thermo-mechanical processing

Processing state	η'(semi-coherent)	η (in-coherent)
Sol+quench (SQ)	Not formed	Not formed
Peak-aged (PA)	5.6	14.5
TMP-1	6.5	5.8
TMP-2	5.8	5.4
TMP-3	5.8	5.4

The highest volume fraction of the η (~8.7%, Table 4.2) was measured in the T6 temper. In contrast, the lowest fractions (~5.4%,) are observed in TMP-3. The high-volume fractions of η' (6.5%, Table 4.2) is calculated for the TMP-2. On the other hand, it was lowest (5.6%) for the T6 temper.

4.2.2 Bulk textures

Fig. 4.2a-b displays 111, 200, and 311 pole figures of the SQ and T6 alloys. The random crystallographic orientation is noticed, and the 111-pole figure displays high intensity compared to the others. Fig. 4.2c portrays 111, 200, and 311 pole figures of TMP-1. Preferred crystallographic orientation is noticed in the 111-pole figure, along a normal direction (ND). Fig. 4.2d depicts 111, 200, and 311 pole figures of TMP-2. Preferred crystal orientation is observed in the 200-pole figure along ND, ensuring the texture development. Fig. 4.2e illustrates 111, 200, and 311 pole figures of the TMP-3. Preferred crystal orientation is noticed in the 200-pole figure along the normal direction (ND), but their intensity is higher than that of the TMP-1 and TMP-2, showing the presence of a strong texture.

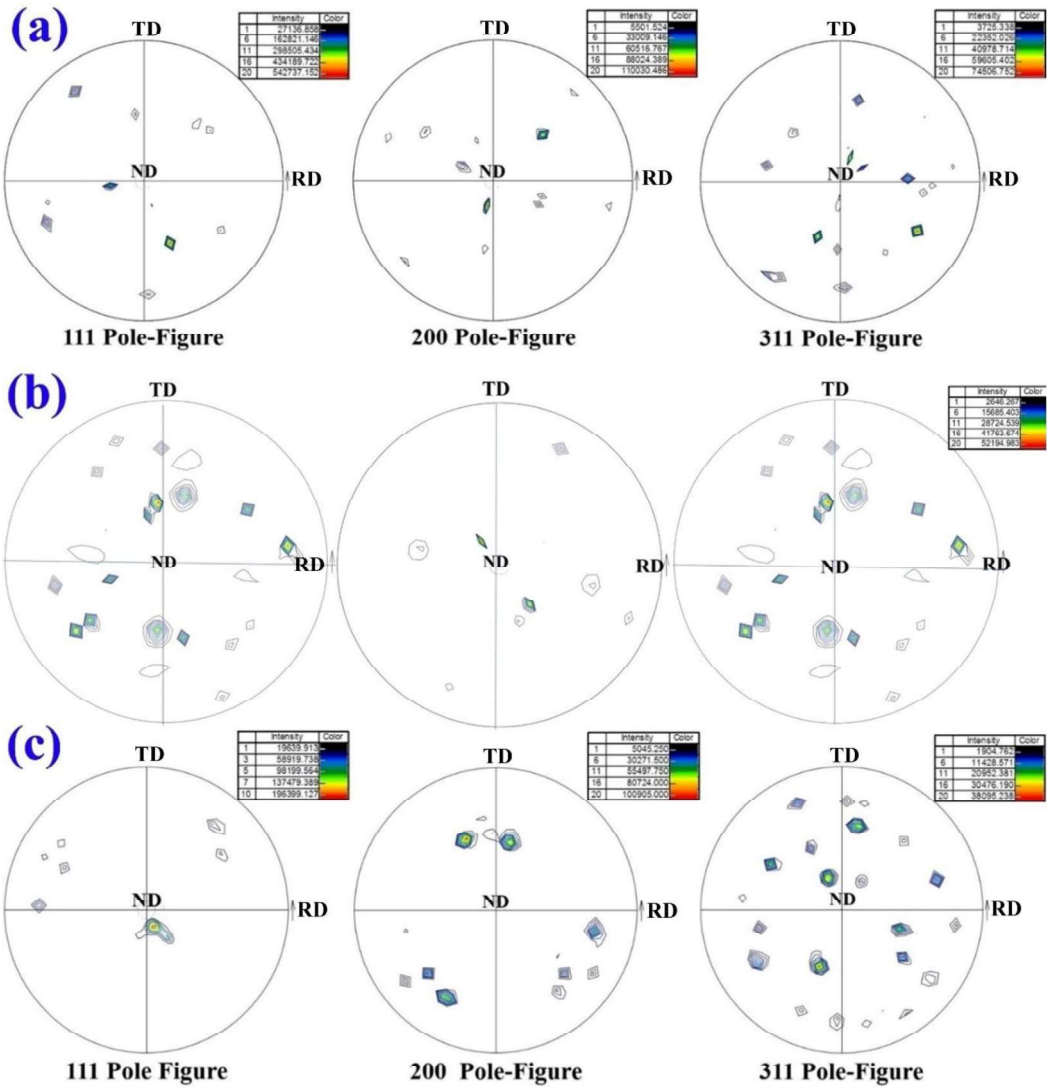

Fig. 4.2a-e. Pole figures, 111, 200, and 220 of: (a) solution quenched (SQ), (b) peak aged (T6), (c) TMP-1, (d) TMP-2, and (e) TMP-3.

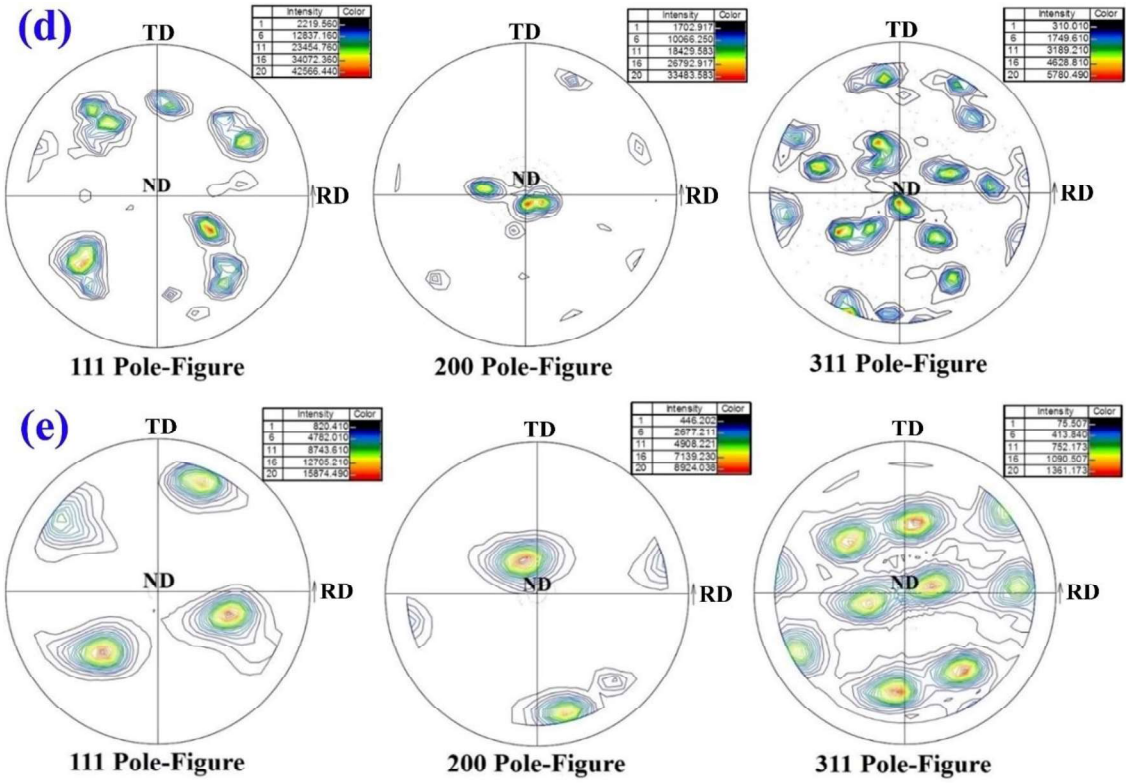

Fig.4.2a-e Continued……

Fig. 4.3a, shows the orientation distribution function (ODF), Φ_2 = 0º, 45º, and 65º sections of the solution quenched (SQ) 7075 Al-alloy. The presence of the α-fiber <011>// ND was noticed respective to Φ_2=0º section, whereas Φ_2 = 45º and 65º sections do not show any texture component. Fig. 4.3b displays the orientation distribution function (ODF, 0º, 45º, and 65º) sections of the peak-aged (T6) alloy. The presence of Goss {011} <100> recrystallization texture is noticed respectively to the Φ_2=0º section. On the other hand, no texture components are seen in the Φ_2 = 45º and 65º sections.

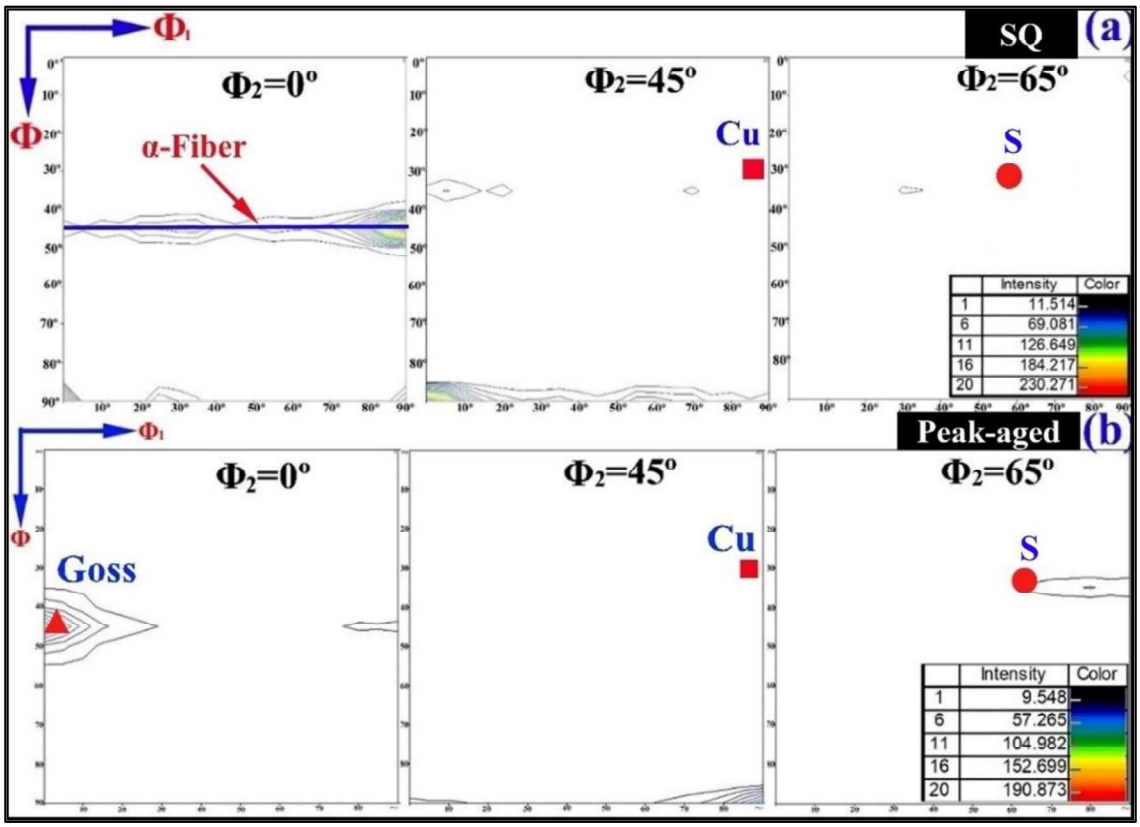

Figs. 4.3 a-e. Orientation distribution function, (ODF) Φ_2= 0º, 45º and 65º sections of (a) SQ alloy, (b) T6 alloy (c) TMP-1, (d) TMP-2, and (e) TMP-3.

Fig. 4.3c depicts, ODF Φ_2 = 0º, 45º, and 65º sections for the TMP-1. The presence of the Cu {112} <111>, and S {123} <634> textures are observed corresponding to the Φ_2 = 45º, and 65º sections but their intensity is more than the SQ and T6 states. The ODF, Φ_2 = 0º section shows an absence of the texture component. Fig. 4.3d represents, ODF Φ_2 = 0º, 45º, and 65º sections of the TMP-2. The presence of the Cu {112} <111>, and S {123} <634> textures are observed corresponding to Φ_2 = 45º, and 65º sections, and their intensities are less than the SQ and T6 tempers. The ODF, Φ_2 = 0º section shows the evolution of the rotated cube {013} <100> textures. Fig. 4.3e shows, ODF Φ_2 = 0º, 45º, and 65º sections of the TMP-3. Presence of the Cu {112} <111>, and S {123} <634> textures are seen respective to the Φ_2

= 45º, and 65º sections. On the other hand, the ODF Φ_2 = 0º section shows a Rotated cube {013} <100> texture, but its intensity is higher than the TMP-2.

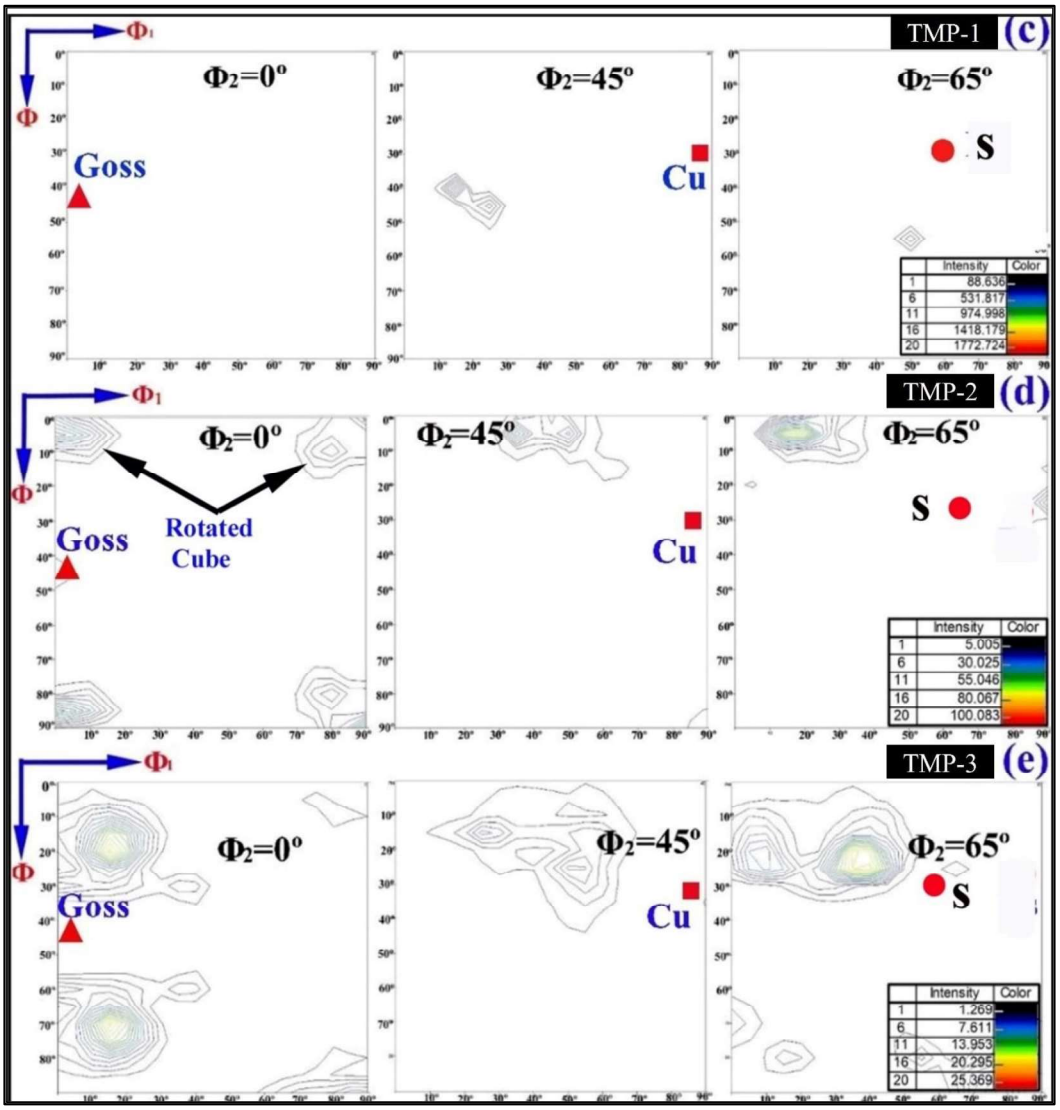

Fig. 4.3a-e Continued……

4.2.3 Micro-texture characterization

Fig. 4.4a shows ODF, Φ_2 = 0º, 45º, and 65º sections for the T6 condition. The Goss {011} <100> recrystallization texture of intensity 14.8 was noticed in orientation 1 respective to the Φ_2=0º section and another texture component with intensity of 3.7 is also seen in

orientation number 2. Rotated goss {110} <110> texture is observed in orientation numbers 3 and 4 at Φ_2=45°section. The ODF, Φ_2= 65º section does not show any texture component. Fig. 4.4b displays ODF, Φ_2 = 0º, 45º, and 65º sections for TMP-1. The presence of the Goss {011} <100> texture with an increased intensity of 20 is observed in orientation 1 of Φ_2 = 0°section. Another texture component with an intensity of 4.8 is observed in orientation number 2. The Cu {112} <11> texture of intensity 20 is rotated to orientation number 3 in Φ_2 = 45°section. The Rotated cube {001} <110> texture is also observed in orientation number 4. The Φ_2 = 65°section does not show texture components. Fig. 4.4c depicts ODF, Φ_2 = 0º, 45º, and 65º sections for the TMP-2. The presence of the Goss {011} <100> texture with an increased intensity of 26 is observed in orientation number 1 of Φ_2=0°section. Another texture component with an intensity of 25 is also observed in orientation number 2. The Cu {112} <11> texture of intensity 20 is rotated to the orientation number 3 in Φ_2 = 45°section. The Rotated Goss {110} <110> texture with an intensity of 25 is another observation in orientation numbers 3 and 4. The Φ_2=65°section does not show any texture components. Fig. 4.4d illustrates ODF, Φ_2 = 0º, 45º, and 65º sections for TMP-3. The presence of the Goss {011} <100> texture with an increased intensity of 28 is observed in orientation number 1 of Φ_2 = 0°section. Other texture components with an intensity of 14, 5.5, and 5.5 are also seen in orientation numbers of 2, 3, and 4 respectively. The Rotated cube {001} <110> texture with an intensity of 5.5 is another observation in orientation numbers 5 and 6 of Φ_2 = 45°section. On the other hand, Rotated Goss {110} <110> texture with intensity of 20 is observed in orientation numbers of 7 and 8. The S {123} <634> texture component with intensity of 5.5 is rotated to orientation number 9 of Φ_2=65° section. Another texture component with an intensity of 14 is observed in orientation number of 10.

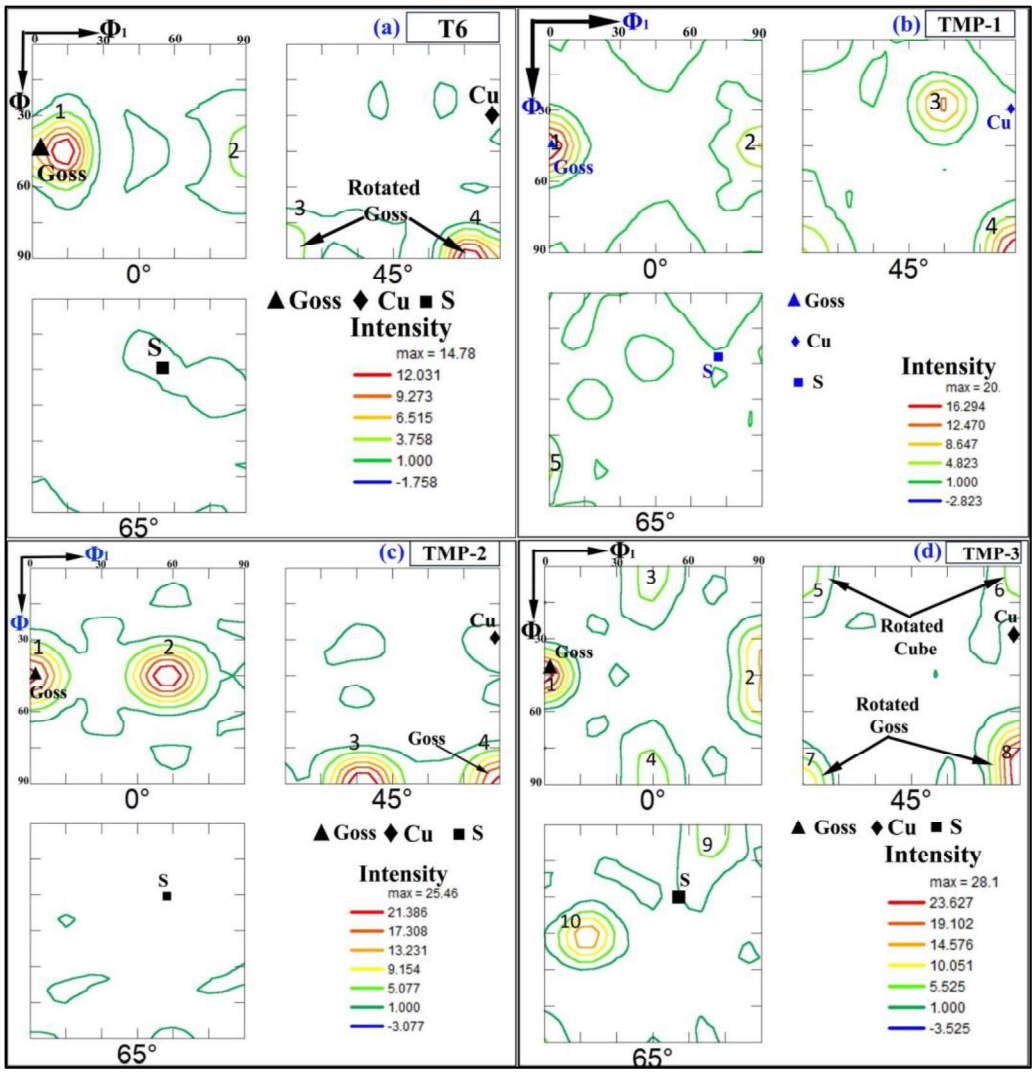

Fig. 4.4a-d ODF, Φ_2 =0°, 45°, 65°sections: T6 (a), TMP-1(b), TMP-2 (c), and TMP-3 (d).

Figs. 4.4.1a-d display superimposed grain boundary maps of the T6, TMP-1, TMP-2, and TMP-3, respectively. The low-angle grain boundary fractions (LAGBFs) in the peak-aged state are 70%, while the high-angle grain boundary fractions (HAGBFs) are 30%. LAGBFs decreased to 68% on TMP-1. On TMP-2, HAGBF decreases to 25%, but then it increases up to 36% in the case of the TMP-3.

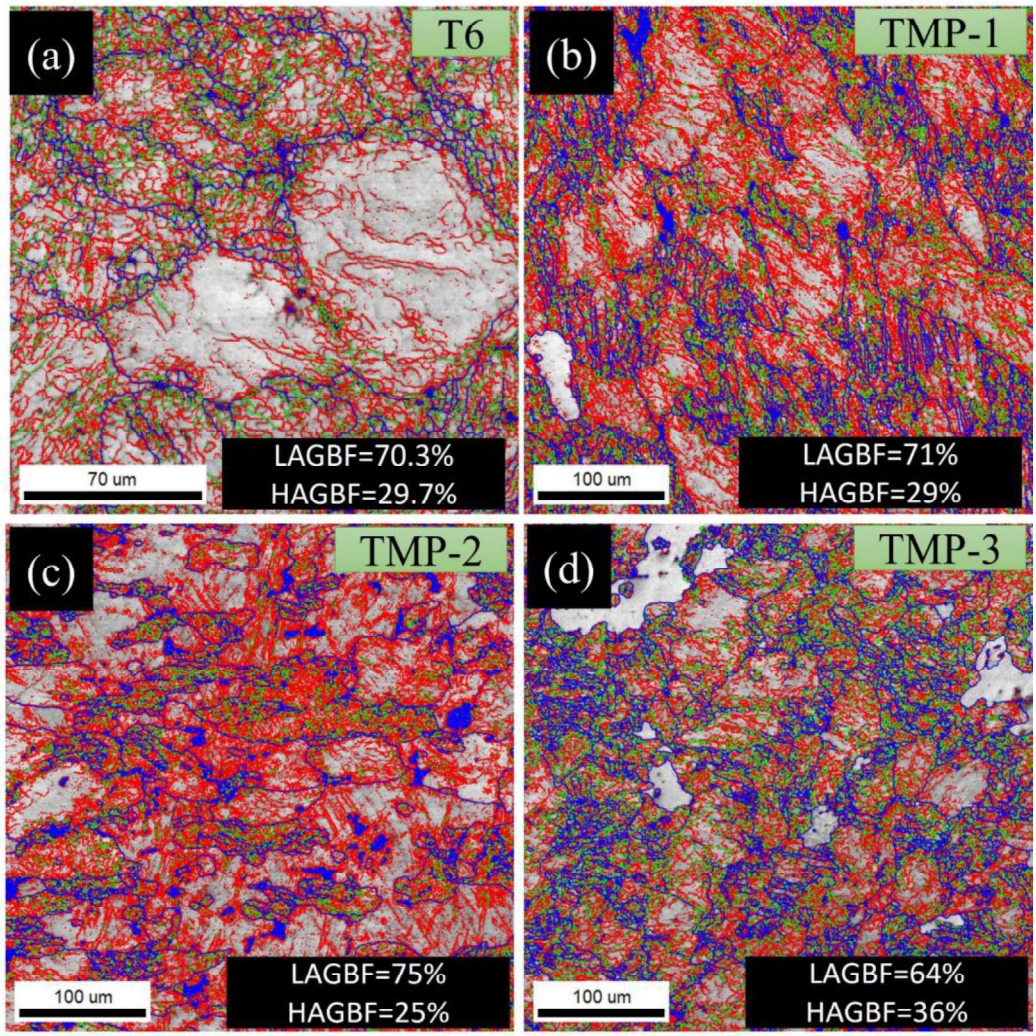

Figs. 4.4.1a-d Super-imposed grain boundary maps for (a) peak-aged (T6), (b) TMP-1, (c) TMP-2, and (d) TMP-3.

Figs. 4.4.2a-d show co-incident site lattice (CSL) boundary fractions for T6 temper alloy as well as those of TMP-1, TMP-2, and TMP-3 alternatively. The co-incident site lattice (CSL) boundary fractions Σ3, Σ5, and Σ9 for peak-aged (T6) alloy are 0.34, 0.10, and 0.19 respectively (Fig. 4.4.2a). After TMP-1, respective CSL boundary (Σ3, Σ5, and Σ9) fractions increased to 0.71, 0.24, and 0.55 (Fig. 4.4.2b). On TMP-2, the Σ3 fractions slightly increased to 0.73. On the other hand, Σ5 and Σ9 boundary fractions were reduced to 0.22 and 0.49. On TMP-3, fractions of Σ3, and Σ5 CSL boundary further increased to 0.79 and 0.9 alternatively. Moreover, fractions of Σ9 boundary decreases to 0.41.

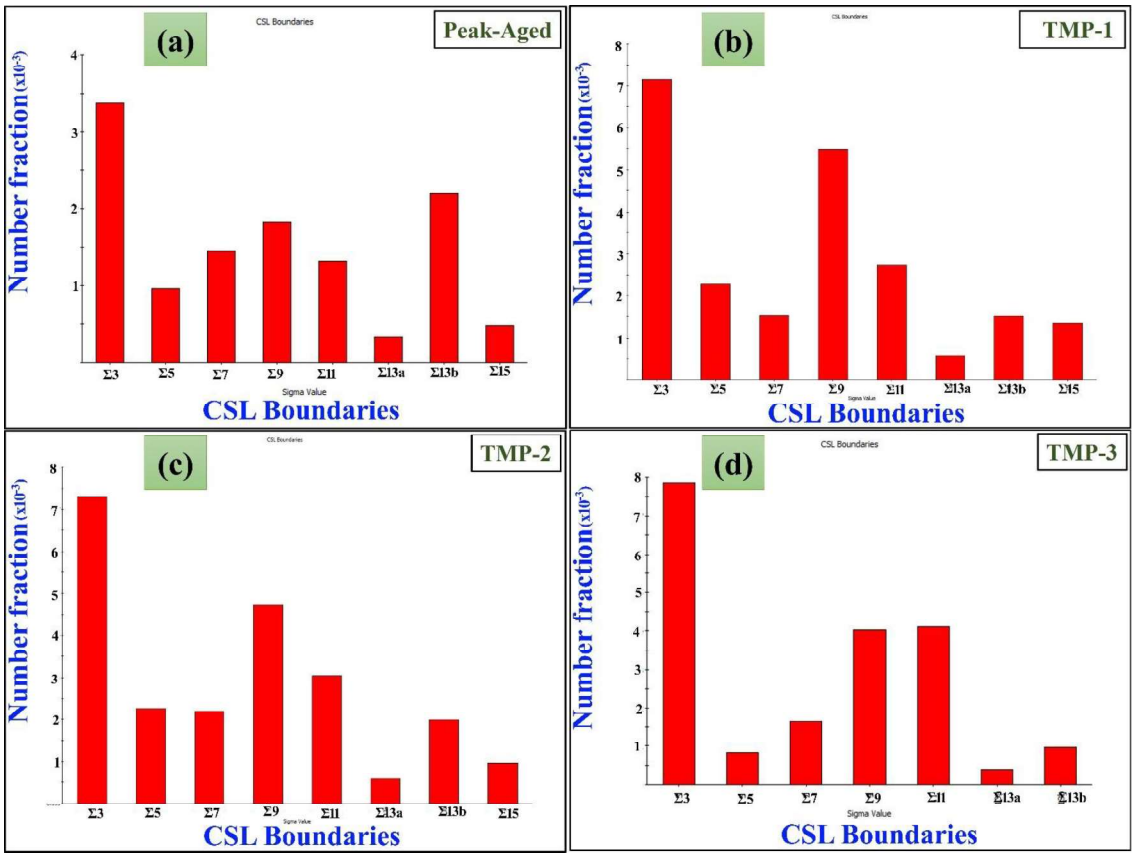

Figs. 4.4.2a-d Co-incident site lattice (CSL) boundary fractions of (a) peak-aged (T6) alloy, (b) TMP-1, (c) TMP-2, and (d) TMP-3.

4.2.4 TEM analysis

Fig. 4.5a shows a bright field TEM image of the solution quenched (SQ) alloy. The presence of the strain field/ dislocation, and absence of metastable precipitates (GP zone, η' and η) were noticed in this. Respective SAEDPs~ are given in Fig. 4.5b. Sharp spots of the α-Al and the absence of the weak spots were observed. Fig. 4.5c depicts a bright field TEM micrograph of peak-aged (T6) alloy. The presence of spherical morphologies of the rod-type features of η', and the plate morphology of η are observed. Corresponding SAEDPs~ are given in Fig. 4.5d. Sharp spots of the α-Al, with six-fold symmetry, and weak spots of precipitates (η' and η) are observed. Fig. 4.5e shows a bright field TEM micrograph of TMP-1. The presence of higher fractions of η as well as dislocation entrapment are observed in the interfaces of η and α-Al matrix. Respective SAEDPs are given in Fig. 4.5f. A linear array of sharp DPs~of α-Al (200) and the absence of the weak spots of precipitates can be seen. Fig. 4.5g shows a bright field TEM micrograph of TMP-2. The coupling effect of dislocation and precipitates is mainly observed. Corresponding SAEDPs are given in Fig. 4.5h. The presence of sharp spots of α-Al are observed but weak spots of precipitates are absent. Fig. 4.5i shows a bright field TEM micrograph after TMP-3. The appearance of the coupling effect of dislocation and precipitates is also observed but the intensity of the coupling effect is more than the TMP-2. Respective SAEDPs are given in Fig. 4.5j. The sharp spots of α-Al are only seen and weak spots attributed to precipitates are absent.

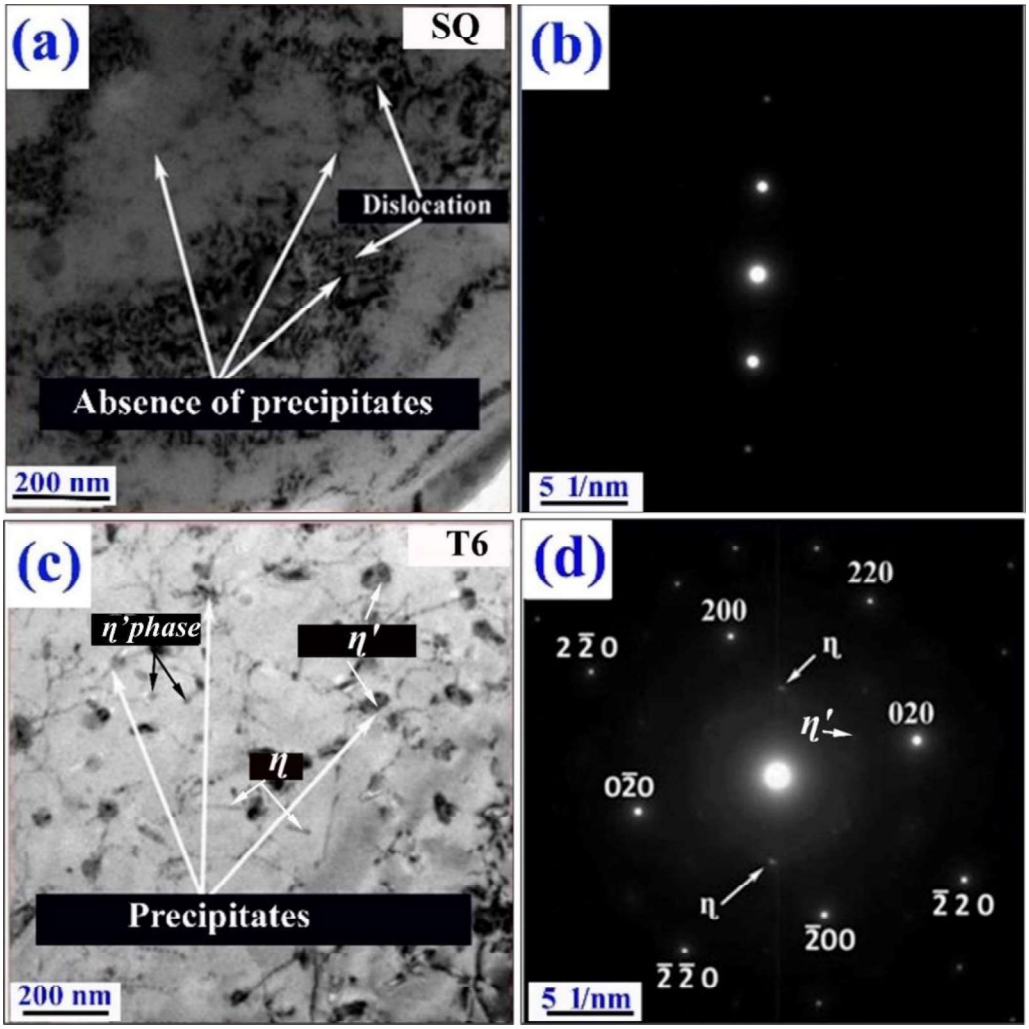

Fig. 4.5a-j Bright field TEM micrograph of SQ and T6 (a,b), and respective selected area electron diffraction patterns (c,d), bright field TEM micrograph of TMP-1, TMP-2 and TMP-3 (e, g, i), corresponding SAEDPs~ (f, h, j).

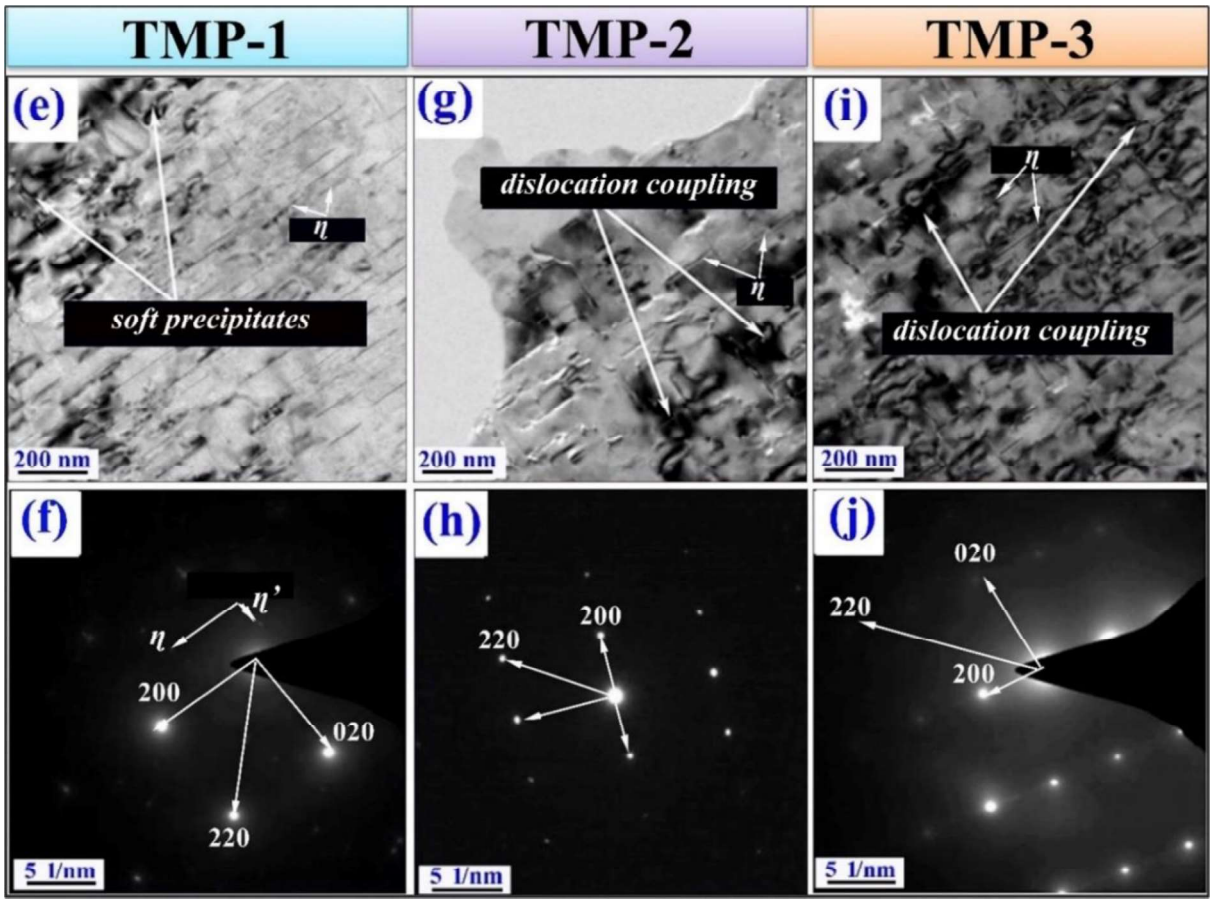

Figs. 4.5a-j Continued……

4.2.5 Nature of precipitates and solute atoms

The Al, Zn, Mg, Cu, and Zr are the most commonly used alloying elements in 7xxx series Al alloys. The Mg is anodic concerning α-Al. On the other hand, Zn, Cr, Cu, and Fe are cathodic [225]. The metastable *(GP zones, and η'),* and equilibrium *(η)* precipitates are also formed in the 7xxx series of Al alloy. The presence of intermetallic, e.g. Al_2CuMg, $Al_2Cu(\theta)$, Al_7Cu_2Fe, and Mg_2Si are also reported in a few pieces of the works of literature [90,91]. The nature of different phases and alloying elements respective to α-Al plays a crucial role in deciding the corrosion performances. The standard corrosion potential value (E°) of α-Al is -767mV. On the other hand, standard corrosion potential values of $MgZn_2(\eta)$, and Al_2CuMg are reported to be 1095 mV, and -1061 mV respectively [91,226]. Similarly, the

(E°) values of Al_7Cu_2Fe, and Mg_2Si are -654 mV and -1536 mV alternatively [91,226]. Therefore, $MgZn_2$ (η) is anodic respective to the α-Al. On the other hand, Al_2CuMg, Al_7Cu_2Fe, and Mg_2Si are cathodic.

4.2.6 Mechanical properties

Fig. 4.6 shows a bar graph of calculated residual stress (in MPa), and hardness (Hv) of the heat-treated (SQ and T6) as well as the thermo-mechanically processed alloy (TMP-1, TMP-2, and TMP-3). Measured residual stress is compressive for all the conditions. The RS for SQ and T6 tempers are -57±8 MPa and -48±5 MPa respectively. The RS values for TMP-1 and TMP-2 are -110±7 MPa, and -158±3 MPa alternatively. On the other hand, the measured RS for TMP-3 is -162±8 MPa. The average hardness for T4, and T6 tempers are 176±5 Hv, and 212±8 Hv alternatively at 100 gm load. On the other hand, the average hardness for TMP-1, and TMP-2 are 159±5 Hv and 171±3 Hv respectively in the same load. The average hardness of TMP-3 is 178±4 Hv.

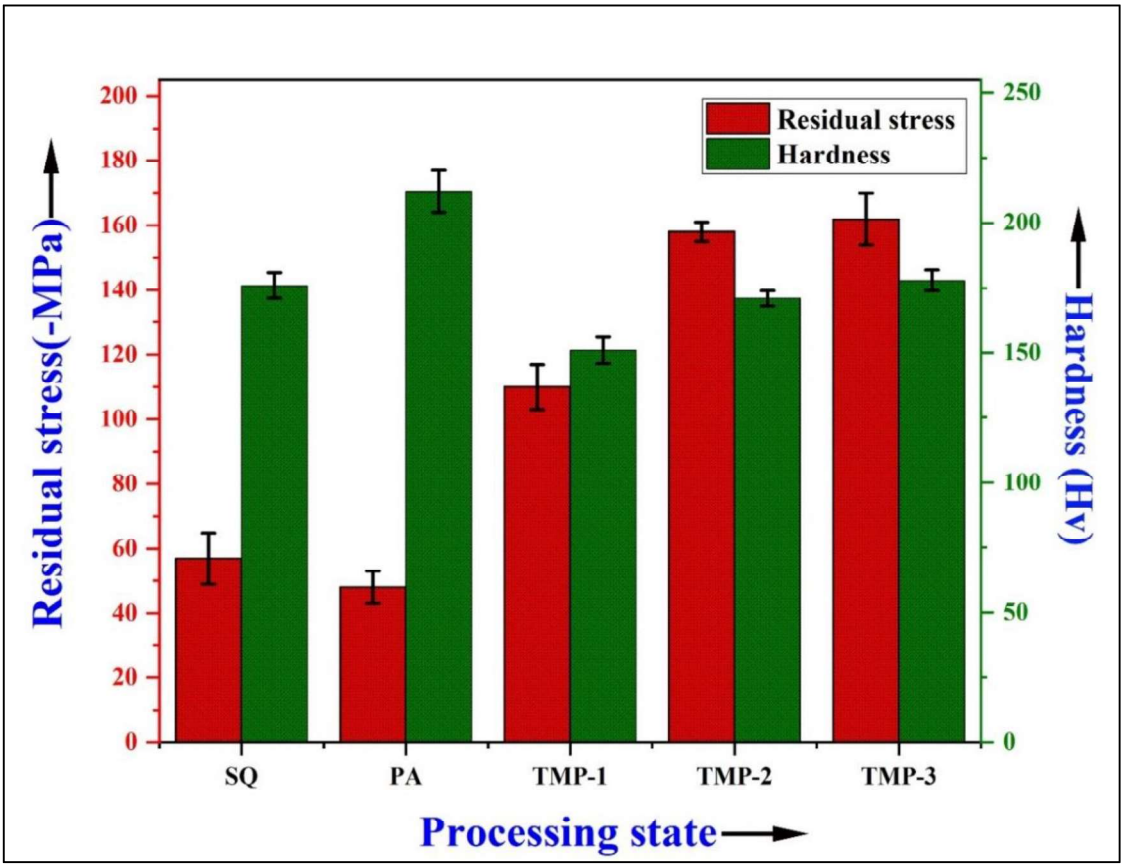

Fig. 4.6. Hardness and residual stress for the T4, T6, TMP-1, TMP-2 and TMP-3 tempered 7075 Al alloy.

Fig. 4.7 displays engineering stress-engineering strain curves of heat-treated (S.Q. and T6) as well as the thermo-mechanically processed alloy (TMP-1, TMP-2, TMP-3). Strain hardening is mainly observed for all the conditions concerning deformation.

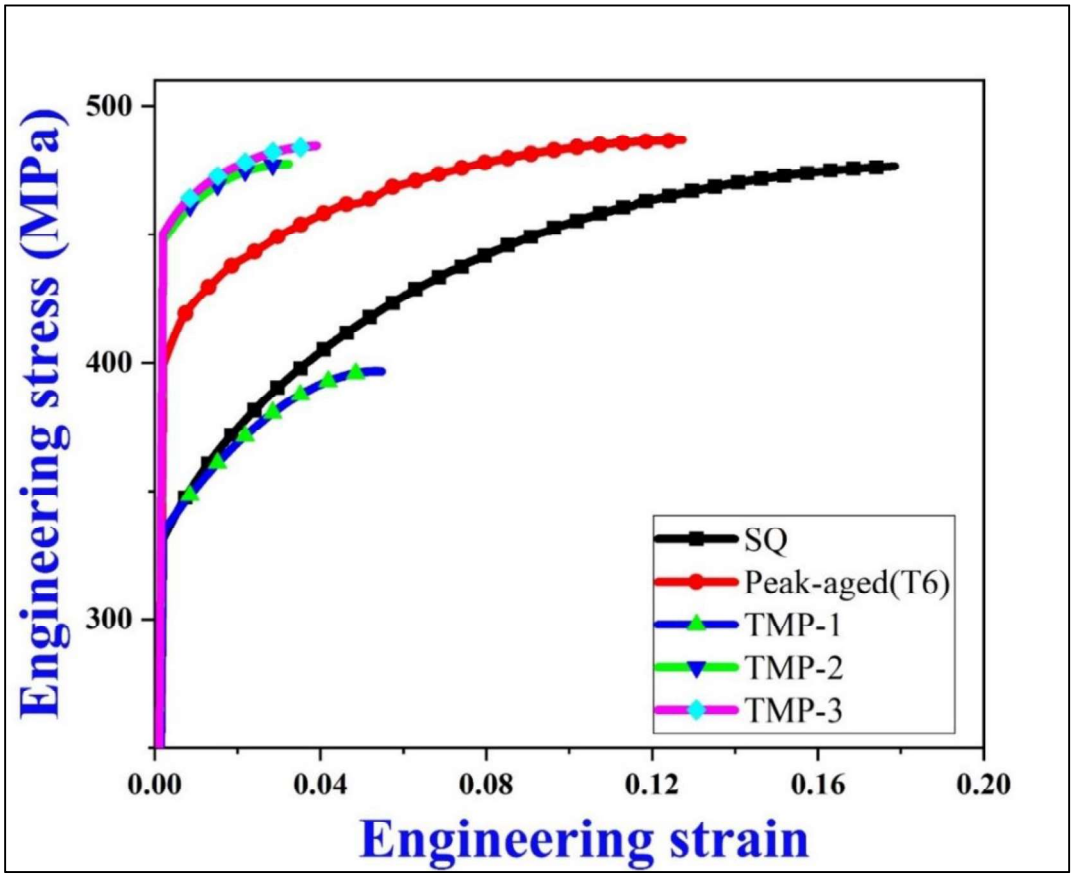

Fig. 4.7. Engineering stress-engineering strain behavior of heat-treated (SQ and T6) alloys as well as TMP-1, TMP-2, and TMP-3.

The tensile properties were calculated with the help of an engineering stress vs. engineering strain plot, and their values are given in Table 4.3.

Table 4.3 Tensile properties of 7075 Al alloy after heat treatments (T4, T6) and thermo-mechanical processing (TMP-1, TMP-2, and TMP-3)

Processing state	**Y.S. (MPa)**	**U.T.S. (MPa)**	**%EL**	**UTS/YS**
Solution quenched (SQ)	330±5	423	18	1.28
Peak aged (T6)	419±12	445	13	1.06
TMP-1	340±7	385	5	1.13
TMP-2	445±5	465	4	1.04
TMP-3	455±10	480	6	1.05

The high UTS (480, MPa) was noticed for TMP-3, which is less than the TMP-1 (385 MPa). The highest percentage of elongation/ ductility was noticed in the SQ state. Moreover, high yield strength (419±12 MPa) was noticed in the peak-aging state (Table 4.3).

4.2.7 Flow behaviors

Using the Levenberg Marquardt Least square regression method, the mathematical relationship proposed by Hollomon [170], Ludwik [171], Ludwigson [172], Swift [173], and Voce [174] are employed for the curve fitting. The best fitting is judged on account of the least chi-square (χ^2) value (sum of squares of the deviation of calculated stress value from the experimental stress value), and highest Adj(R^2) value (coefficient of determination or goodness of fit).

Figs. 4.8a-e displays log true stress vs. log true plastic strain curves of SQ, T6, TMP-1, TMP-2, and TMP-3. All the curves display an upward concave shape except the Hollomon and the Voce relationships. The Hollomon [63], equation results in a linear fit. On the other hand, much deviation was noticed from the experimental plot, after fitting the Voce [174] equation.

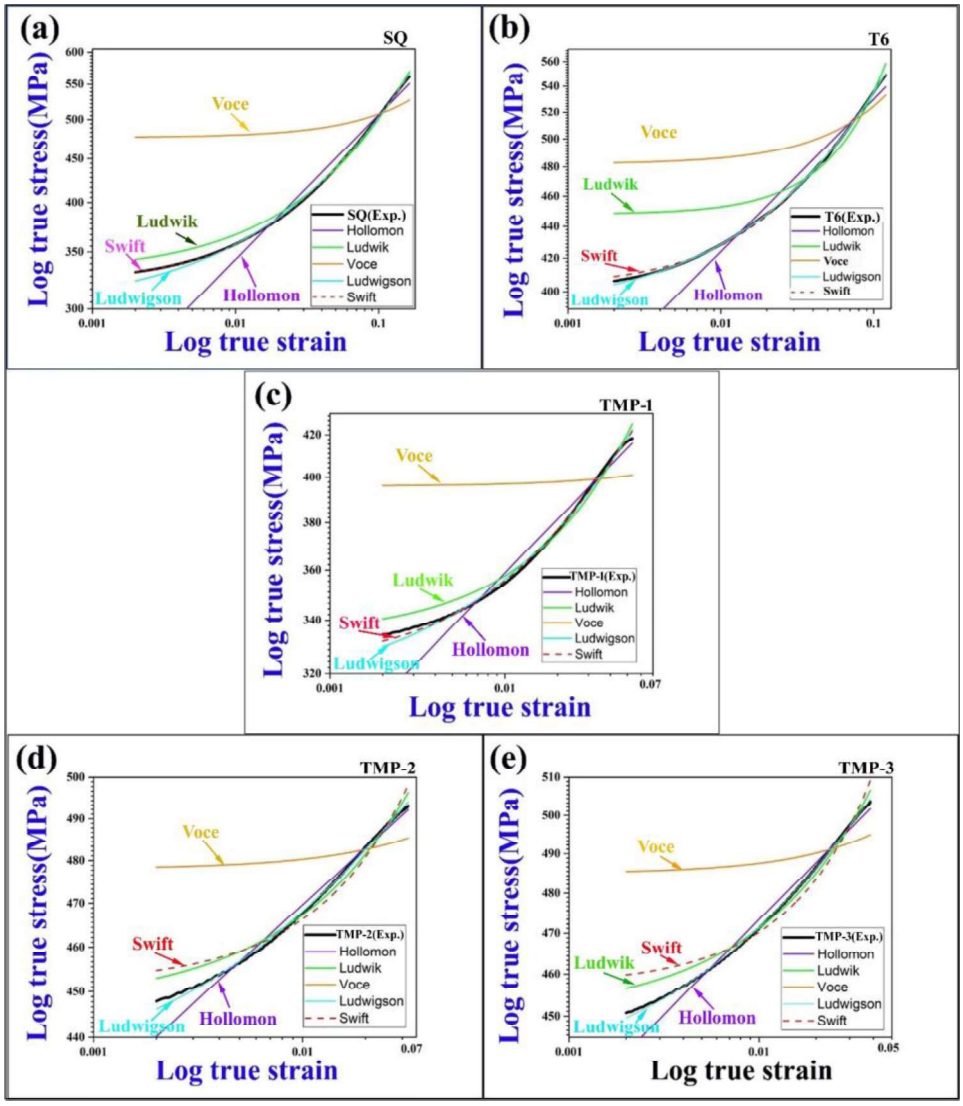

Fig. 4.8a-e Fitted flow curves using mathematical models: (a) SQ, (b) T6, (c) TMP-1, (d) TMP-2, and (e) TMP-3.

The alloys in the SQ, T6, and TMP-1, show one of the best fittings with a Swift equation $(\sigma = K(\varepsilon_0 + \varepsilon)^n$, Figs. 4.8a-c). In contrast, TMP-2 and TMP-3 display the best fittings with a Ludwigson equation $(\sigma = K_1\varepsilon^{n1} + exp(K_2 + n_2\varepsilon)$, Fig. 4.8d-e) with two different sets of the hardening exponents (n_1, n_2), as well as the strength co-efficient (K_1, K_2), but their flow curve parameters are different which is recorded in Table 4.4.

Table 4.4 Flow parameters of the best-fitted mathematical models of heat-treated and TMP

Temper schedules	**Strength co-efficient (K, MPa)**	**Hardening exponent(n)**	**Flow curve behavior**	**Adj(R^2)**	**(χ^2)**
S.Q.	832.5	0.26 *(n),* and .024 *(ε_0)*	Swift $\sigma = K(\varepsilon_0 + \varepsilon)^n$	0.99987	0.5185
T6	771	0.18 *(n),* and .025 *(ε_0)*	Swift $\sigma = K(\varepsilon_0 + \varepsilon)^n$	0.9974	0.4798
TMP-1	651	0.16 *(n),* and 0.13 *(ε_0)*	Swift $\sigma = K(\varepsilon_0 + \varepsilon)^n$	0.9974	1.273
TMP-2	K_1 = 911, K_2 =6.06	n_1 = 0.62, n_2 = -3.32	Ludwigson $(\sigma = K_1\varepsilon^{n1} + exp\ (K_2 + n_2\varepsilon))$	0.9988	189
TMP-3	K_1= 873, K_2=6.07	n_1 = 0.63, n_2 = -2.7	Ludwigson $(\sigma = K_1\varepsilon^{n1} + exp\ (K_2 + n_2\varepsilon))$	0.9845	621

The strain hardening exponent *(n)* of the SQ and T6 alloys are 0.26 and 0.18, respectively, and corresponding pre-strain *(ε_0)* values are *~0.24 and 0.25* (Table 4.4). The Adj(R^2) values of both curves are close to 1(0.99967), and their reduced chi-square *(χ^2)* values are very low, 0.5185 and 0.4798, respectively, showing one of the best fittings with flow curves. The strain hardening exponent *(n),* and pre-strain *(ε_0)* value for TMP-1, are ~0.16 and 0.13, respectively, and the Ajd(R^2) value is very close to 1, but the reduced chi-square *(χ^2)* value is very less ~1.273, showing one of the best fittings of flow curves. Moreover, TMP-2 and TMP-3 display best fitting with the Ludwigson *($\sigma = K_1\varepsilon^{n1} + exp\ (K_2 + n_2\varepsilon)$)* flow curve. This indicates the two different deformation mechanisms followed by the two different types of dislocation structures evolution in the lower and higher strain regimes. The strain-hardening parameters for TMP-2 and TMP-3 in the low-strain regimes were n_1 = 0.62 and n_1 = 0.65, respectively. The strain hardening exponent (n), in high strain regime for both the alloys are: *n_2 =-3.32, and n_2 = -2.70* (Table 4.4). The strength coefficient (K) for TMP-2, in low strain

regime, is, K_1=*911 MPa*, which is measured to be K_2 = *6.06 MPa*, in the high strain regime. For specimen TMP-3, the strength co-efficient in the high and low strain regimes, K_1 and K_2 are *873 MPa, and 6.07 MPa* respectively. The Adj(R^2) values, of both the alloys, were close to 1 (*0.9988 and 0.9845*), and chi-square (χ^2) values are least ~189, and 621 respectively (Table 4.4.), displaying one of the best fittings with flow curves.

Figs. 4.9a-c displays the log-log plots of hardening rate $(d\sigma/d\varepsilon, \theta)$ vs. corrected true plastic strain $(\varepsilon_0+\varepsilon)$ for the SQ, T6, and TMP-1 tempers alternatively that is best fitted with the Swift relationship $(\sigma = K(\varepsilon_0+\varepsilon)^n)$. The SQ alloy depicts four stages of hardening rate ($d\sigma/d\varepsilon, \theta$), corresponding to corrected true plastic strain $(\varepsilon_0+\varepsilon)$ (Fig. 4.9a) but TMP-2 and TMP-3 (Fig. 4.9b-c) show three stages of hardening behavior.

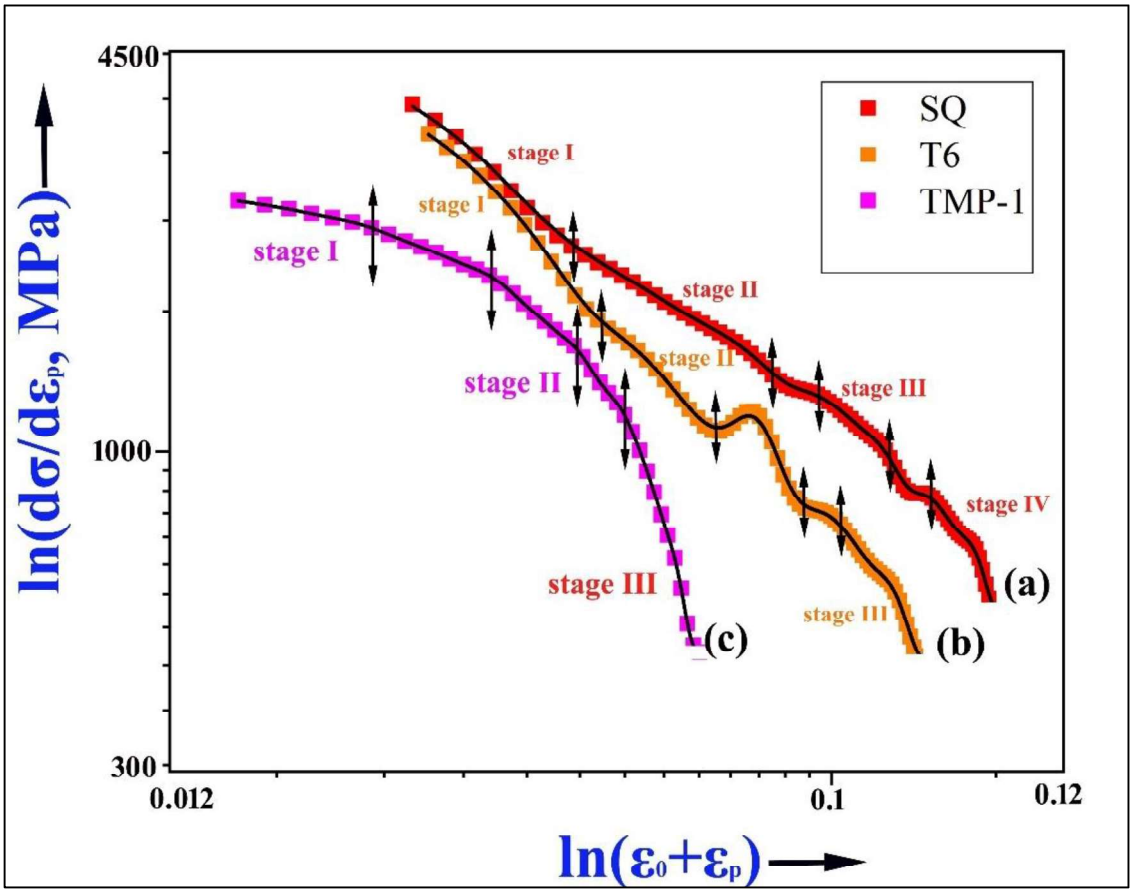

Figs. 4.9a-e Logarithmic hardening rate, $ln(d\sigma/d\varepsilon_p)$ versus true plastic strain $ln(\varepsilon_0+\varepsilon_p)$ plot of the Swift fitted curves (a,b,c), and Ludwigson fitted curves (d,e).

The magnitude of the slope (n-1), transition strain (ε_r), and strain hardening rate (Θ) for all the stages were determined by applying the linear curve fitting method, and the derived parameters are given in Table 4.5.

Table 4.5 Magnitude of the slopes, and hardening rate of the Swift fitted curve

Materials	**Slope** ***(n-1)***			**Work hardening rates** ***(Θ, MPa)***			
	I	**II**	**III**	Θ_1	Θ_2	Θ_3	Θ_4
SQ	-1.06	-0.7	-1.03	2112	1453	996	673
T6	-1.34	-1.2	-1.4	1582	1108	572	
TMP-1	-0.24	-1.0	-4.5	2330	1189	504	

For SQ alloy, stage I shows a gradual decrease in hardening rate *(Θ)* concerning the corrected true plastic strain *($\varepsilon_0+\varepsilon$)* (Fig. 4.9a). Stage II further displays a decreasing trend, but their rate is slower than stage I. Stage III pertains to the softening stage, where the hardening rate *(Θ)* decreases gradually concerning *($\varepsilon_0+\varepsilon$)* but at a rate faster than stage II. The IV stage is the softening stage but the rate of decrease is very sharp in comparison to the others. At the end of stage-II, and stage III there is a range of transition strain *(ε_r= 0.083 to 0.096),* and *(0.125 to 0.1337)* respectively (Fig. 4.9a).

For T6 temper, stage-I shows a gradual decrease of hardening rate *(Θ)* concerning the ($\varepsilon_0+\varepsilon$) with the transition a stage at slightly higher true strain (Fig. 4.9b). Stage-II, again shows a decreasing rate *(Θ),* but the decreasing trend is sharper than SQ. There is a wide range of transition strain between stage-II, and stage-III beginning of which displays a transition true strain *(ε)* of 0.0715. Stage-III, again shows decreasing *Θ* concerning *($\varepsilon_0+\varepsilon$),* and decreasing behavior is faster than the T4. The magnitude of the slope *(n-1)* in Stage I is -1.39 which is less than stage II (-1.4) & stage III (-1.56). The transition true strain *(ε_r),* at the end of stage I, II, and III are 0.0484, 0.0715, and 0.11 respectively (Fig. 4.9b).

The TMP-1, again depicts a decreasing hardening rate in stage I, with a wide range of transition strain (ε_r), at beginning of the stage II (Fig. 4.9c). Hardening rate (θ), further decreases in stage II and stage III, but the rate is higher in stage III, as compared to stage II.

On the other hand, the decrease in stage III is very sharp. The magnitude of the slope *(n-1)* in stage I is -0.24, which is less than that of stage II (-1.03) and stage III (-4.05) (Fig. 4.9c). There is a range of transition true strain (ε_r), at the end of stage I (0.024 to 0.033), and stage II (0.045 to 0.058). At the end of stage III, the transition true strain is 0.064 (Fig. 4.9c).

For the SQ specimen, the hardening rate (Θ), at the end of stages, I, II, III, and IV are 2112 MPa (Θ_1), 1453MPa (Θ_2), 996 MPa(Θ_3), and 673 MPa(Θ_4) (Fig. 4.9a). The hardening rate of T6 temper is Θ_1= 1582 MPa, at the end of stage I, Θ_2 = 1108 MPa, at the end of stage II, and Θ_3= 572 MPa, at the end of stage III (Fig. 4.9b). The TMP-1 depicts a hardening rate of Θ_1 = 2330 MPa, at the end of stage I, Θ_2 = 1189 MPa, at the end of stage II, and Θ_3 = 504 MPa, at the end of stage III (Fig. 4.9c).

Fig. 4.9d-e shows the hardening rate **($d\sigma/d\varepsilon$, Θ)** vs. true plastic strain **(ε_p)**, for TMP-2 and TMP-3, which is best fitted with the Ludwigson curve. Three stages of hardening behavior are also noticed in this. Stage I, displays sharp/ concave decreasing behavior. Stage II shows a slight dip and hump feature but stage III depicts a linear decreasing trend concerning true plastic strain *(ε_p).* The hardening rate (Θ), and transition true strain were calculated at the end of every stage. But slope and intercept values are calculated for stage III, because of a linear decreasing trend of Θ *concerning with a* ε_p.

The hardening rate (Θ) of TMP-2, at the end of stage I is Θ_1= 3299 MPa, at the end of stage II, is Θ_2 =1647 MPa, and Θ_3 = 1002 MPa, at the end of stage III (Fig. 4.9d). The transition strain (t_r) at the end of Stages I, II, and III are 0.012, 0.021, and 0.035 respectively. The alloy TMP-3, depicts a hardening rate, *of* Θ_1 =3038 MPa at the end of stage I, Θ_2=1337 MPa, at the end of stage II, and Θ_3 =889 MPa, at the end of stage III (Fig. 4.9e). The transition strain true strain (t_r), at the end of stages I, II, and III, are 0.012, 0.021, and 0.028 alternatively.

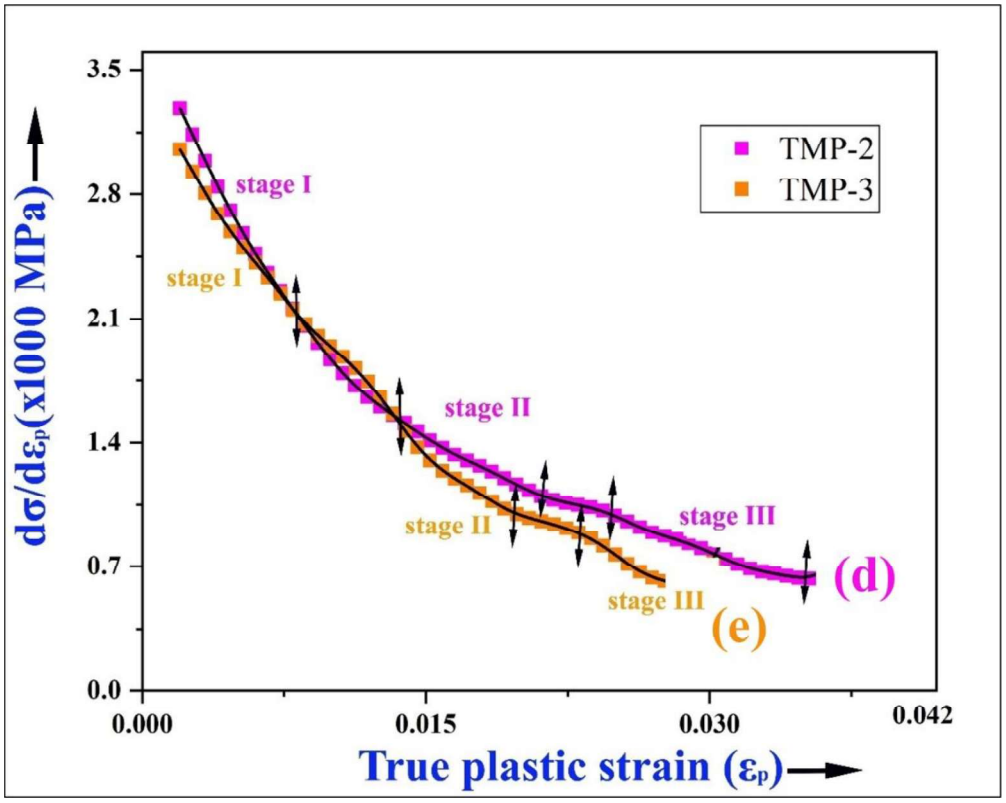

Fig. 4.9a-e. Continued…….

The slope *(m)* and intercept (Φ_0) of the linear portion of stage III of TMP-2, and TMP-3 are calculated using the polynomial fittings, and their values are given in Table 4.5.

Table 4.6 The slope, intercept, transition strain *(ε),* and hardening rate *(Θ)* of the Ludwigson fitted flow curves.

Materials	**Slope (n)& Intercept in stage III**		**Transition true strain *(ε_r)***			**Work hardening rate *(Θ, MPa)***		
	Intercept *(Θ_0)*	Slope *(m)*	ε_1	ε_2	ε_3	Θ_1	Θ_2	Θ_3
TMP-2	1934	-38322	0.012	0.0211	0.062	3299	1647	1002
TMP-3	2348	-63128	0.011	0.0203	.0283	303	1337	889

The magnitude of the slope of a linear fitted curve in stage III of TMP-2 is -38322 *(slope, m),* and the intercept *(Θ_0)* is 1934. For TMP-3 the magnitude of the slope is -63128 *(m),* and

the intercept is 2348. The Adj(R^2) value of the linear fitted curve is close to 1 (0.9932 in stage 1 and 0.985 in stage 2), and the chi-square (χ^2) value is the least showing one of the best-fitted flow curves.

4.2.9 Fractography analysis

Figs. 4.10a-d displays fracture morphologies of the solution quenched (SQ) and the peak-aged (T6) alloys. Dimples and facets were reported in the solution quenching state (Fig. 4.10a-b). Micro voids, dimples, and intergranular cracks were noticed in the peak-aging (T6) state (Fig. 4.10c-d). The average dimple size in the SQ state is 11± 2.8µm (Fig. 4.10a-b), which is more than the T6 alloy (4.8± 1.0 µm, Fig. 4.10c-d).

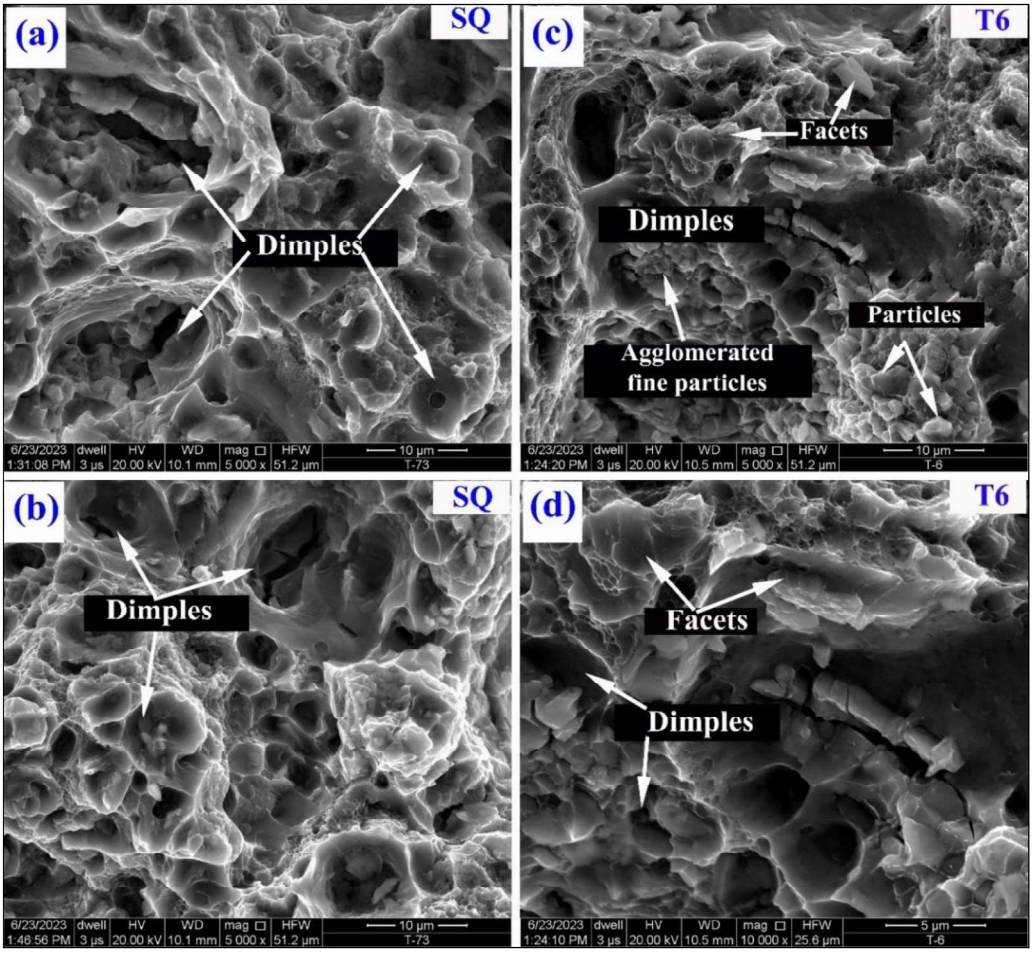

Fig. 4.10a-d SEM micrograph fracture surface of (a,b) SQ alloy, and (c,d) peak-aged (T6) alloy.

Figs. 4.11a-f show fracture surface after thermo-mechanical processing (TMP-1, TMP-2, and TMP-3). The presence of the micro-voids, and dimples are major observations but their size is different. The average dimple size for TMP-1 is 8.0±2.0 μm (Fig. 4.11a-b), which is more than the TMP-2 (5.3±1.0 μm, Fig. 4.11c-d), and TMP-3 (7.0±1.8 μm, 4.11e-f). The dimples are uniformly distributed in TMP-3, as compared to the TMP-2, and TMP-1. The depth of dimples for TMP-1 is higher than the TMP-2, and TMP-3, and they follow the order of dimple size as TMP-1 > TMP-3 > TMP-2.

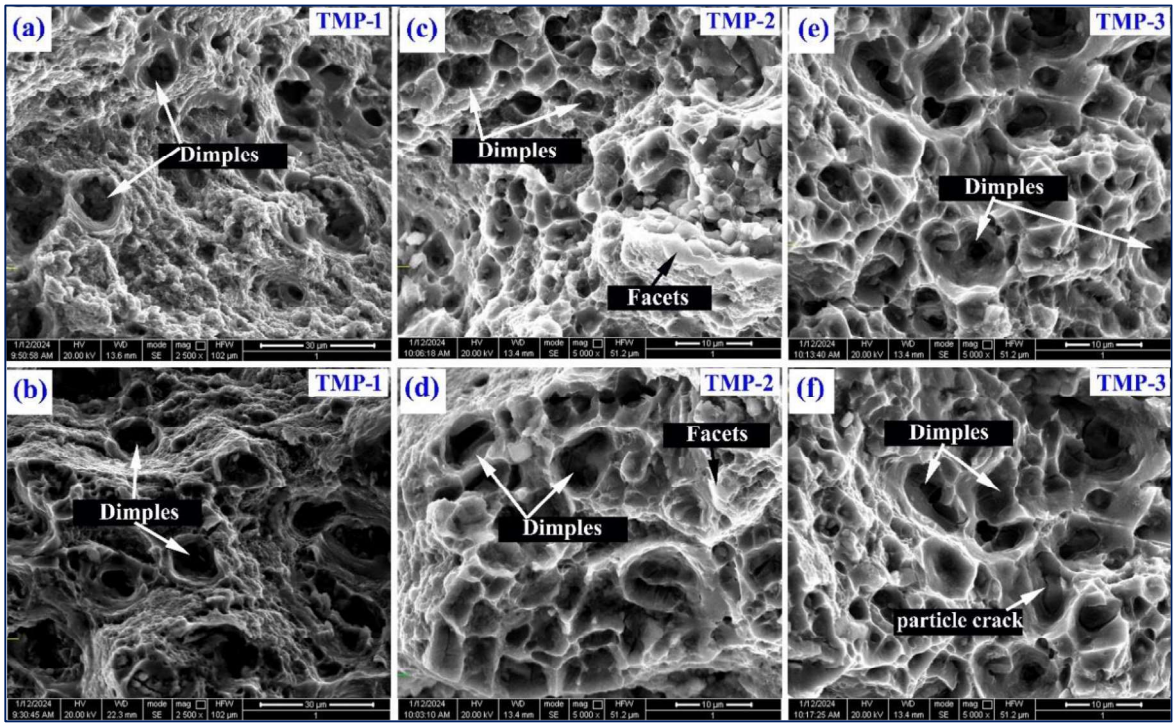

Figs. 4.11a-f. Fracture surface after TMP: (a, b) TMP-1, (c, d) TMP-2, and (e,f) TMP-3.

4.3 Discussion

Absence, of the metastable (GP zone, η'), and equilibrium (η) precipitates in SQ alloy (Fig. 4.1a, and Fig. 4.5a) arises because room temperature aging is not enough for the decomposition of supersaturated solid solution (SSSS) in α-Al [71]. On the other hand, the formation of such precipitates in T6 temper occurs due to diffusion-assisted nucleation of precipitates, because ageing temperature (>120ºC) is enough for the decomposition of SSSS (α)[71]. The pipe diffusion and dislocation sweeping mechanisms play an important role in such precipitation [21]. Changes in the lattice parameter of α-Al (200 peaks shifted towards the right) also support the formation of precipitates in the alloy matrix. An increased fraction of η and soft phase in TMP-1 arises due to deformation-assisted increased vacancy concentration which directly influences the diffusion kinetics. The increased dislocation density accelerated the pipe diffusion paths thereby diffusion rate of solutes from SSSS(α) [227]. The glide dislocation during plastic deformation collects the solute atoms from α-Al, by sweeping mechanisms thereby promoting the accelerated η(Table 4.2) formation by the pipe-diffusion mechanisms [187]. Therefore, dislocation sweeping and pipe diffusion play an important role in the formation of ηin TMP-1 (Table 4.2) as per the facts reported in the literature [228]. The increased fraction of η' and η, after TMP-2 and TMP-3 (Table 4.2) arise due to enhanced dislocation density dominated structural phase transformation, from the GP zone to η' in the first stage. In contrast, η' to η in the next stage. Left shifting of 111 peak positions of α-Al, concerning deformation also supports changes in the lattice parameter thereby lattice misfit or enhanced dislocation density after TMP. Changes in crystallographic orientation from 111 of α-Al to 200 of α-Al also support texture development in the processed alloy. Formation of the α-fiber at $\Phi_2 = 0°$ is a characteristic feature of texture development in SQ or heat-treated alloy (Fig. 4.3a) [111]. Evolution of Goss {011} <100>,

and Cube {001} <100> recrystallization texture are characteristic features of the peak-aged (T6) alloy [31]. Chen et al. [31], also reported Goss {011}<100>, and Cube {001}<100> texture after subjecting the alloy to peak aging. Such textures are the signature of the deformation texture and formed due to enhanced dislocation density thereby significantly influencing the SCC, and cyclic loading performances of alloys [31]. Taking the amount of deformation into account, the intensity of Brass (Bs) texture increases concerning deformation increasing the dynamic recovery by activation of the non-octahedral slip system **[220 A].** Moreover, the decreased intensity of S {123} <634> texture in the current investigation (Fig. 4.3 d and e) is because S {123} <634> texture requires low stored energy of deformed alloys or requires strain relaxation path for grains to grow. Crystallographic planes in 111, 200, and 220 pole figures of α-Al, are randomly distributed for SQ and T6, along the RD, TD, and ND showing the development of random texture. Moreover, the increased intensity of the 111-pole figure of TMP-1, and the preferred orientation of the 111-crystal plane along ND, also support the texture development. Changes of the crystal orientation from 111 of α-Al, in TMP-1, to 200 of α-Al, after TMP-2, and TMP-3 justify the evolution of the deformation textures. For instance, Bs, S, and Copper textures, etc, further change the orientation or become unstable due to the ageing treatment. The XRD analysis (Figs. 4.1a-e) also confirms such an observation. The interfacial energy of nucleating precipitates determines the precipitation sequence of the age hardenable 7xxx series of Al-alloy [183]. On the other hand, the shape and size of precipitates are governed by the mathematical relationship proposed by Nabarro [120]. In this relationship, the function, Φ(c/r) ratio, mainly determines the shape of precipitates. The spherical precipitate form arises because Φ(c/r) ratio is 1 for the spherical precipitate of GP zone, 0.75 for rod type of η' precipitates, and the ratio is far less than 1, for the η precipitates [76]. It is also reported

that the formation of spherical morphology is a characteristic feature of the GP zone. On the other hand, rod and plate morphologies are respective features of the η' and η as observed in T6 temper (Fig. 4.5b). Increased spherical precipitates of the η in a localized area of TMP-1 (Fig. 4.5c) are due to increased dislocation density dominated by enhanced diffusion of solute atoms that form the η precipitates. The presence of a greater number of weak DPs~ in Fig. 4.5h supports the enhanced formation of η phase. The increased dislocation density provides short-circuit diffusion paths for the nucleation of a η' and η. Due to increasing deformation, structural phase transformations occur from the GP zone to η' and η' to the η at TMP-2 and TMP-3 (Fig. 4.5d and e), respectively. Due to the shear-resistant nature of η' and η, mobile dislocation provides a coupling effect between dislocation and precipitates in the α-Al on account of increased deformation. The absence of weak spots of precipitates also supports the coupling effect of dislocation and precipitates. The ageing after deformation increases nucleation sites for the precipitation, accelerating the formation of precipitates. The low-angle grain boundaries are corrosion and crack-resistant [31]. On the other hand, high-angle grain boundaries cause ductility. Therefore, slightly increased HAGBFs (32%) for TMP-1 will cause more ductility than TMP-2 because their HAGBFs are 25%, but their ductility will be less than the T6 condition due to deformation-dominated enhanced dislocation density. On TMP-3 ductility further improves because their HAGBFs increase by up to 36%. The low CSL boundaries ($\Sigma 3^n$) are stress corrosion cracking (SCC), and crack resistant. Simultaneously it also improves the failure caused by the fatigue and hydrogen embrittlement (HE) **[181 A].** Therefore, increased CSL ($\Sigma 3$) boundary boundaries after thermo-mechanical processing ($\Sigma 3 = 0.71$, 0.73, and 0.79 for TMP-1, TMP-2, and TMP-3) in comparison to the peak-aging (T6) ($\Sigma 3 = 0.34$) would likely help to obtain the corrosion and crack resistant alloy **[181 B].**

Less strength and high ductility in the case of the SQ alloy are due to the absence of precipitates (Figs. 4.5a-b). Precipitates free matrix causes less barrier effect for a motion of dislocation in the α-Al matrix, thus resulting in high ductility and less strength. Diffusion-assisted formation of the GP zone, η' and η precipitates in T6 temper (Fig. 4.5c-d) provides a barrier effect for dislocation motion in the α-Al matrix thereby increasing the strength and hardness. The strengthening effect depends on the nature of the interface and the size of the strengthening precipitates. The smaller but coherent precipitates are sheared by the dislocation. On the other hand, large precipitates are cut through dislocation and bypassed. Less strength in TMP-1 is due to the increased formation of a coherent GP zone (Figs. 4.5e-f), which provides a less barrier effect for the dislocation motion. The coupling effect between the dislocation and precipitates in TMP-2 (Figs. 4.5g-h), and TMP-3 (Figs. 4.5i-j) are the major responsible factor for enhancement in the strength of alloys. Enhanced ductility arises due to dislocation recovery on account of ageing. On the other hand, high strength is caused by the coupling effect of dislocation and precipitates in the bulk matrix. The strength of TMP-1 is less due to the increased volume fraction of the soft phase (Table 4.2). On the other hand, strength increases but ductility decreases for TMP-2 (Table 4.2), because of enhanced precipitation of the η' phase (Fig. 4.5g-h). The TMP-3 further increases the strength and ductility (compared to TMP-2) due to the coupling effect of dislocation and precipitates of η (Fig. 4.5g and i). The upward concave shape of log true stress vs. log true plastic strain curves (Fig. 4.8a-e) is due to the strain hardening effect on account of plastic deformation. The best-fitted Swift equation, in the case of the SQ, T6, and TMP-1 depicts the presence of pre-strain in alloys. More pre-strain (ε_0) in SQ alloy is due to super-saturated solid solution or absence of precipitates (Fig. 4.8a-b) which creates lattice micro-strain in α-

Al. Slightly reduced pre-strain (ε_0~0.22) for T6 (Table 4.4) arises due to the formation of the transition (η'), and equilibrium (η) precipitates (Fig. 4.8c-d).

Further, reduced pre-strain (ε_0) for TMP-1 (Table 4.4) is due to accelerated precipitation of the soft phase in comparison to η' and η which creates less lattice misfit in the α-Al thereby the pre-strain. The two-slope deformation behavior on account of the best-fitted Ludwigson curves, for the TMP-2 and TMP-3 arise due to coupling effect of dislocation and precipitates in α-Al (Fig. 4.5g and i). The coupling effect is due to the shear-resistant nature of the η' and η. The strong coupling effect of TMP-3 in comparison to TMP-2 arises due to enhanced precipitation of the shear-resistant η phase. The dislocation loops/forest dislocation observed in some portions of the alloy matrix/dislocation-free region causes less resistance for the dislocation motion thus producing less hardening effect in the alloy. This is about the deformation behavior in the low strain regime (n_2 = -3.32 for TMP-2, and n_2 = -2.7 for TMP-3). Whereas, the coupling effect of dislocation and precipitates as observed in Figs. 4.5g, i. This strongly stops the dislocation motion thus resulting the high hardening. The less coupling effect of the dislocation and precipitates in TMP-2 (Fig. 4.5g-h), causes a low strain hardening exponent in the lower strain regime (n_1 = 0.61).

The strong coupling effect between dislocation and precipitates in TMP-3 (Fig. 4.5i-j) results in high hardening (n_1 = 0.65, Table 4.4) in comparison to TMP-2. The coupling effect of dislocation-precipitates activates the multiple slip system on account of the plastic deformation thereby increasing the strain hardening effect. The sharp decrease in hardening rate *(Θ)* in stage I of SQ and T6 alloys is due to the absence of a barrier effect in the initial stage of deformation. Further, a slow decrease in the hardening rate in stage II arises due to the barrier effect created by dislocation-dislocation interaction in SQ, in addition to the barrier effect produced by the dislocation and precipitates in T6. The slope of T6 in stage II

is higher because the hardening rate (Θ) decreases due to the combined effect of the dislocation and precipitates. The range of transition strain (Tr), at higher sites, is due to the presence of the coarse non-shearable (η) precipitates. A steep decrease in stages III and IV of the SQ and T6 alloy is due to the recovery mechanisms. The slow decrease in stage I of TMP-1 is due to the accelerated precipitation of the soft phase. On the other hand, a large transition strain (Tr) at the beginning of stage II arises, due to the presence of a coarse precipitate, and enhanced interparticle spacing. The moderate decrease in hardening rate in stage II is due to the activation of the multiple slip system. A steep decreasing behavior of a hardening rate in stage III is due to recovery mechanisms. Dislocation pile-up and cellular dislocation structures are the characteristic microstructural features in this stage.

The sharp decrease in Θ in stage I is due to the absence of a barrier during the initial stage of deformation. The slow decrease in hardening rate in stage II is due to the presence coupling effect of dislocation and precipitates which stops the dislocation motion during plastic deformation. The slope of stage II in TMP-3 is more due to the enhanced hardening effect provided by the strong coupling of dislocation and precipitates (Fig.4.5i). The linear but slow decrease of hardening rate (Θ) in stage III of TMP-2 and TMP-3 could be best explained with the help of the Kock, Mecking, and Esterin (KME) [199,200] based dislocation model which is given by Eq. 4.1:

$$\beta = d\sigma/d\varepsilon_p = \Theta_0 + m\sigma \quad \text{.....Eq. 4.1}$$

Here, β = strain hardening rate in stage III, σ = true stress (in MPa), m is the slope of the linear portion, and constant Θ_0 = dislocation storage term. In Eq.1 high value of Θ_0 indicates high dislocation storage capacity and a high negative value of m depicts the low dynamic recovery during tensile plastic deformation. The high Θ_0 value of TMP-3 (2348, Table 4.5) displays a more dislocation storage capacity than the TMP-2 (1934). A more negative m

value of TMP-3 (-63128) in comparison to TMP-2 (-38322) illustrates the less dynamic recovery. Therefore, the range of stage III is low in TMP-3, in comparison to TMP-2.

The formation of dimples and facets (Fig. 4.10a-b) in solution-quenched (SQ) alloy is due to the combined effect of the ductile and the brittle failure mode [90,229,230]. The inter-granular fractures, micro-voids, and dimples at T6 temper (Fig. 4.10c-d) depict the fracture along the grain boundaries and indicate the ductile mode of failure. Voids and dimples observed in TMP-1 also depict the ductile failure mode (Fig. 4.11e-f). Micro voids, and dimples in TMP-2 (Fig. 4.11g-h) support the ductile failure mode. In contrast, reduced dimple size, and shear facet indicate reduced ductility but enhanced strength. Uniformly distributed dimples with slightly increased size show enhanced elongation/ ductility in the case of the TMP-3 (Fig. 4.11i-j).

4.4 Conclusions

1. XRD results confirm the high-intensity reflection of 111 peaks at 15% CR, 200 reflections at 30%, and 45% cold deformation respectively during thermo mechanical processing.
2. High-intensity texture components were observed corresponding to 111 pole figures at 115% cold deformation and 200 pole figures at 30% and 45% cold deformation but the intensity of 200 pole figures at 45% cold deformation is high as compared to the 30% cold deformation i.e. materials do not change the preferred orientation of the 200-crystal plane beyond the 30% cold deformation.
3. Solution quenched (SQ) and peak-aged (PA) alloy display recrystallization texture components whereas, thermo-mechanically processed specimen illustrates fiber texture components of TMP-1 specimen. On the other hand, intense rotated Cube, and rotated Goss, along with fiber components were other features found while increasing the deformation at TMP-2 and TMP-3.
4. Residual stress values are compressive. However, the compressive-ness decreases, and the hardness increases concerning cold deformation.
5. Thermo mechanical treatment improves the strength ductility trade-off due to the coupling effect of the dislocation and precipitates.
6. The best fitting with Swift equation of SQ and T6 alloy shows the presence of pre-strain in materials. On the other hand, the best fitting with the Ludwigson equation shows the two-slope deformation behavior.
7. Formation of the coherent precipitates and dislocation loops and forest dislocation structure is attributed to the low strain regime, whereas the coupling effect of dislocation and shear-resistant precipitates cause high hardening in the alloy.